We thank the reviewers for their careful and detailed comments, which have greatly improved the manuscript. Below is our response to these comments; reviewers' comments are in normal font; **our responses are in bold font.** Line numbers in blue refer to the "latexdiff" comparison of the revised manuscript with the original manuscript, appended at the end of this response.

Reply to the Anonymous Referee #1

In this manuscript, Xie et al. run an offline mineral dust emission model forced by a significant suite of climate model simulations that look at the broad stripes of climate change across the Phanerozoic. Based on the results of these simulations, it is argued that the principal driver of dust emission across the Phanerozoic is the degree of continentality, i.e., times when there are big continents across the subtropics. Greenhouse gas levels are of minimal import. The manuscript compares its results with the distribution of evaporite records and finds some agreement ("fair" used in the abstract may be overly generous), which is considered sufficient validation of the model. I will note that the results about the broad movements in Phanerozoic climate align well with the results of Hu et al. (2023, https://doi.org/10.1038/s41561-023-01288-y) on monsoon strength, possibly because the underlying model experiments use similar approaches.

We have changed the wording from "fair agreement" to "reasonable agreement" in the abstract and the conclusion in the revised manuscript. Line 16, 498.

The work presented in this manuscript is a valuable contribution to our understanding of the geological record of dust by providing a sort of null hypothesis testable against that record: that dust emission (and the level of global deposition) are driven mainly by variability in hydroclimate (and factors directly related to hydroclimate such as vegetation cover). The experiments presented in the manuscript are suitable to provide this null hypothesis. The manuscript is clearly written and well-organised. However, the manuscript takes little account of research on the geological record of dust, either in the recent or deep past. The outcome is that evaporite distribution is used as a proxy for dust emission. However, this type of validation is circular. Evaporite deposition is, of course, more demonstrably controlled by hydroclimate and continentality. So, of course, a model that has a response strongly controlled by hydroclimate and continentality is going to match the distribution of evaporites quite well.

We clarified in section 5.1 revised manuscript that we are not considering evaporites as a proxy for dust emissions. Instead, we are using evaporite distribution as a method for evaluating the hydrological cycle in the model. The idea of the validation is that because there are limited geological records that can directly represent dust emissions, we instead here carry out an indirect comparison to evaluate our climate model simulations which drive the dust model. The simulated evaporites from HadCM3 are compared to the evaporite records, and this model-data comparison is intended to evaluate the performance of HadCM3 in simulating the hydrological cycle. Because our analysis shows that the dust emissions are controlled by arid regions, this is an important, albeit indirect, evaluation of the modelling framework. We do not believe that there is any circularity here. Lines 375-388.

The alternate hypothesis that these simulations should allow to be tested once further work is done to characterise the geological record of dust through time is that dust emission through time is a balance between two, sometimes competing factors. First, dust is mostly produced by physical weathering in glacial margin environments rather than "just there" or forming from the collision of desert sands. Second, dust is most easily emitted in dry, but not too dry environments, where vegetation cover is minimal but crusting together of small particles by evaporite salts is also minimal or reduced by occasional re-wetting. The upshot of this hypothesis is that dust emission increases gradually in icehouse climates as sediment availability increases, peaks in the early part of greenhouse climates (or in states of higher global continentality) following an icehouse climate, and then wanes through the course of long eras of greenhouse climate, as the dust (technically silt-sized sediment) reaches long-term sediment sinks, like the ocean. Because glacial grinding is a contested process, it is therefore very helpful to have a modelling study that removes the sediment from the equation and looking at change across the Phanerozoic. But it would be best if the manuscript gave the reader better information about the alternate hypothesis and the observables in the geological record. I therefore recommend that this manuscript be published after revision to better review the deep time geological record of dust and consider the inconsistencies the modelling approach in the manuscript might have with even the relatively recent record of dust.

We agree that weathering related to glaciation could potentially play an important role in dust emissions through its impact on surface particle availability. However, testing the importance of this factor requires higher-resolution data of glacial movement and melting, as well as topography, of the Earth's deep past, which is very limited in availability. In the revised manuscript, we added literature that highlights this important mechanism, both from modern observations and paleo studies, and clarified our model cannot directly test this hypothesis. We also suggested future research based on this limitation. Lines 49-51, 58, 107-111, 486-488.

I will focus first on how the modelling in this manuscript looks in the light of geological evidence from the Holocene and Pleistocene, provide some useful background on ongoing work in reconstructing the deep time record of dust, and then provide some minor comments on the manuscript line by line. The model in this manuscript is one of atmospheric dust emission. By tuning to the AMIP models, the manuscript is strictly speaking only treating the dust sizes (0.1-10 μm) typically represented in the AMIP models on the grounds of their relevance to atmospheric radiation/clouds and presence in dust deposition records distal from emission (such as ice cores). See Mahowald et al. (2006 , https://doi.org/10.1029/2005JD006653) or Mahowald et al. (2014, https://doi.org/10.1016/j.aeolia.2013.09.002) for further discussion of these points.

We clarified the particle size our model takes into consideration by referring to the parameterization of the AMIP models that we are turning to. Lines 206-208.

However, the best proxies for the geographic distribution of dust emission are proximal deposits of dust, where particle sizes are bigger (and much of the mass is concentrated geologically). These are known as loesses and can be 10s or sometimes 100s of m thick. Loesses typically have particle sizes ~50 µm. Thus, if the approximate atmospheric dry deposition lifetime of 5-10 µm is 1.7 days (Mahowald et al., 2006), the lifetime of loess particles is ~ 1 hour. Remobilisation complicates the picture, and the nature of sedimentary geology is for sinks to be few at any one time. But the upshot is that the geological record of dust emission is strongly concentrated within the bounds of wherever the wind can blow dust in a few hours (~ 100 km). So when faced with a figure showing the world's loess deposition in recent sediments, any model that connects dust emission to hydroclimate etc. rather than sediment availability is faced with a problem. (See Fig. 2 of https://doi.org/10.1016/j.earscirev.2019.102947) for a good example. Loess is abundant in mid-latitude and some high-latitude areas across North America and Eurasia, South America and parts of Australasia that include New Zealand. And it is relative rare along the southern margin of the Sahara. The model presented in the manuscript might explain the rarity of Saharan loess for the most recent time slice. (But where are the Pliocene loesses in the Sahara contemporary with the Eurasian ones?) But North American loess, European loess, and New Zealand loesses are inexplicable. This observation is the motivation for the idea that dust emission is shaped by sediment availability, with sediment primarily being generated by physical weathering at glacial margins (see discussion in Mahowald et al., 2006 and Prospero et al., 2002, https://doi.org/10.1016/j.earscirev.2019.102947).

The manuscript certainly demonstrates limited knowledge of dust records through geological time. At line 49, it says, "similar orbital-driven dust (or aridity) records are also identified much further back in time, as early as the Late Cretaceous 50 (Niedermeyer et al., 2010; Vallé et al., 2017; Zhang et al., 2019)." In fact, the most widespread evidence for orbitally-driven dust deposition is from the Late Paleozoic. A good place to start would be a recent review by Soreghan et al. (https://doi.org/10.1144/SP535-2022-208) and probably too recent for the authors to see (https://doi.org/10.2110/jsr.2023.122). The work by Lynn Soreghan suggests loess deposition was widespread, even at low latitudes in late Carboniferous and early Permian Pangaea. Loess also seems widespread in much of the Permian (where we can see), not just in places Soreghan and her collaborators have looked but in Russia (Mouraviev et al., 2015, doi: https://doi.org/10.1134/S0031030115110064). Loess deposition certainly continues deeper into the long greenhouse interval (see Chan et al., 1999, https://doi.org/10.2110/jsr.69.477), but the Triassic peak in dust emission by the model seems inconsistent with the record, where the places we would expect to see loesses are mostly sandstones and evaporites.

Many thanks to the reviewer for providing useful references on the paleo dust records; we made use of this suggested reference and improved the review of dust records. Lines 49-51, 58, 108.

For the inconsistency mentioned by the reviewer regarding the Triassic peak: The location (approximately 54°W, 17°N, rotated according to the GPlate model for the upper Triassic continent) where loess sediment was identified by Chan et al., 1999, is simulated to be an area where evaporites could form (see plot for 218 Ma in Figure A6). We do not believe this indicates an inconsistency between our simulation and geological records. Firstly, the spatial resolution of our simulations is significantly different from the actual length of the cross-section where the loess is found. Therefore, for a grid box where the model predicts evaporite, we cannot assume that the entire land area of that grid box is covered by evaporite. Similarly, we cannot deny the possibility that loess may exist within that grid area. Secondly, both the sediment

record and model simulation times are approximations, both around 218 Ma, with considerable uncertainty regarding the exact age. Therefore, we cannot conclude there is an inconsistency based on the fact that the absolute ages of the sediment record and model simulation do not precisely align.

I still do agree with the general thrust of the manuscript that the deep time record of dust is poorly understood, but this should not be done without emphasising the importance of loess as a proxy for dust emission, some more expanded references to work in this area, and more nuance when comparing the model results with evaporite distributions.

Minor Comments

Line 47: This is probably where sediment availability and glacial grinding should appear as a hypothesis. Additional possible references are: Reader et al. 1999 (https://doi.org/10.1029/1999JD900033) and Sugden et al. (2009, https://doi.org/10.1038/ngeo474)

We added words about sediment availability and reference in the corresponding paragraph. Lines 49-51, 58.

Line 100: Omitting the Zender et al. formulation is justifiable if you are clear that you are trying to help test between hydroclimate/meteorology and sediment supply hypotheses.

We have made it clearer in the revised manuscript that our model simulations cannot test the sediment supply hypotheses. Lines 108-111, 486-488.

Figure 1: The notation of units in the legend/colorbar is confusing. Normally, you don't superscript the exponential notation, so there's a clear distinction between e-09=10^-9 vs. e^-9

We have corrected the notation of units in figures.

Line 339: Desert has become dessert

Corrected.

Fig. A4 Part 3: 213 Ma looks like a plotting error. Please check.

We have corrected this error in the revised manuscript.

Reply to Referee #2 Yonggang Liu

Xie et al. develop and tune a new offline dust emission model, DUSTY, based on which and the climate simulations they have carried out previously, a continuous model-derived timeseries of global dust emissions over the whole Phanerozoic is established. The simulation results provide quantitative insights into significant fluctuations in dust emissions during this Era. Notably, the study highlights the dominant influence of non-vegetated areas on dust emissions. The authors further investigate the mechanisms underlying the hydrological variations, governs the aridity the distribution non-vegetated areas. The findings demonstrate that paleogeography serves as the primary driving force behind dust emission variations, while the role of CO_2 is found to be marginal. The comparison between the simulated region of dust emission and the distribution of evaporite sediment records is not bad given the uncertainties in so many boundary conditions and model parameters. The manuscript provides new knowledge to both geologists and paleoclimatologists and clearly written in general, I recommend publication after a relatively minor revision.

Major comments

1. More detailed comparison should be made here of the 15_MMM and 0Ma simulations, which are crucial for tuning and evaluating the model. Although the model parameters of the DUSTY model have been optimized by maximizing the Arcsin Mielke score and the global mean emissions are the same, significant differences still exist between Figures 1a and 1b. For example, the dust emission in the middle of Eurasia and South America is seriously underestimated while that over Australia is highly overestimated. Are they due to biases in the simulated climate, vegetation or dust parameterization? The implication to the simulated distribution of dust emission in other periods should also be discussed.

   The comparison between the tuning target (Figure 1a) and the tuned pre-industrial simulation (Figure 1b) indicates that the DUSTY model can represent the general spatial distribution of dust emissions. However, biases exist in the detailed distributions. It represents our simulations fail to capture the small-scale areas with very high emissions (hot spots). We added contents in section 3.2. And expand the similar potential discrepancy in section 4.1. Lines 248-254, 275-277.

2. The absence of land plant colonisation before 410Ma implies that the inclusion of vegetation cover during 541-410Ma in this study may have resulted in an underestimation of dust emission during this period. The influence of this effect on the major conclusions of their study should also be discussed.

   The TRIFFID vegetation scheme, coupled with the GCM, employs a simple representation of terrestrial vegetation, incorporating five plant functional types that cover a broad climate range. This simplification introduces a bias for early Paleozoic periods before the colonization of land plants, resulting in our simulations predicting both bare soil and vegetation where, in reality, there would

have been only bare soil. Consequently, this leads to an underestimation of dust emissions during those periods.

We carried out further simulations to constrain the underlaying uncertain and added this discussion to the limitations in Section 5.2. The underestimation is also added to the conclusion. Lines 447-462, 497.

Specific Comments

Line 45-48: May add "glaciogenic rock powder" or other equivalent expressions.

We added contents about sediment availability. Also clarified in the revised manuscript that our model simulations cannot test the sediment supply hypotheses. Lines 49-51, 58, 107-110

Line 188-190: is the global mean the average over all the land or over the regions with nonzero dust emission?

The global mean is calculated over the entire global area, including both land and ocean. This approach ensures consistency when comparing the means across different time slices and avoids confusion arising from variations in the total land area over time.

Line 189: 'C1' should be changed to 'C2'. This correction is also required in Table 1.

Both are corrected.

Line 230: It should be added here that the results are from the S2 series of experiments.

We added clarification. Line 260.

Line 282-285: How was the value of 0.8 mm/day chosen here? The bracket at the end of Equation 10 needs to be removed.

We added reference on choosing this value. And the extra bracket has been removed. Lines 318-319.

Reply to the Editor Yannick Donnadieu

Technical points to start:
• You say that the dust model requires high-frequency outputs, but it remains difficult to understand how these outputs are used to calculate the different parameters and why it is not possible to do so with monthly outputs.

The GCM outputs used to run the dust model in this study are of hourly resolution, rather than monthly. This is because dust emissions have a cubic dependence on windspeed, and so it is important to capture short timescale variations in windspeed in order to correctly simulate dust emissions.

• In addition, how are the C constants estimated? Are they calculated point by point or is it a global average value?

We clarified the coefficients in section 2.1. They are all calculated at a global mean level. **Lines 126-129.**

• Is there a CO_2 fertilization effect on continental vegetation? And if so, what is the effect on the prediction of arid areas for past times with high CO_2 concentrations?

Yes, the vegetation model TRIFFID sees the varying CO_2. Thus, we should see fewer non-vegetation areas for past times with high CO_2 concentrations. It would be possible to explore this further, with a sensitivity study in which the TRIFFID model saw a constant CO_2, but this is beyond the scope of this manuscript. We added discussion on this aspect of uncertainty in section 4.2. **Lines 469-475.**

• For climate simulations with constant CO2, does the solar constant vary?

Yes, the solar constants used to drive the simulation series with constant CO2 varies the same as other simulation series. We have added sentences in section 2.3 to clarify. **Lines 176-177.**

• Figure 6 is cited in the text after Figures 7 and 8, please change the numbering.

Changed.

Two moderate points:
• Why not directly analyze the outputs of the vegetation model, in particular the distribution of arid areas? Why calculate an aridity index when the climate model can give you direct access to arid areas? In this logic, would it be possible to directly plot the evolution of arid areas from the vegetation model? The last sentences of the conclusion suggest that the evolution of dust flux would only be linked to the continents that cross the subtropical arid

zones, it is not that simple and geometric. Figure 8 shows very well that the major increase in dust flux is also a consequence of the collapse of the tropical humid zone between 280 and 190 Ma. Atmospheric and oceanic circulation diagnostics are missing to provide an explanation for the reasons for the disappearance of the tropical humid zone.

We do see similar patterns of the non-vegetated-area evolution to the evolution of arid areas. The primary causal relationship is likely that the aridity leads to lack of vegetation, but there is also of course dynamic feedback from the vegetation to the climate. As such, showing the aridity index as a way of explaining the non-vegetated areas is appropriate.

We added interpretations to explain the collapse of tropical humid zone that seen during the supercontinent times, and this is largely due to the albedo related feedback. Lines 165-169, 354-358.

• Can you explicitly write the numerical method used to predict evaporites from your model? From my understanding of evaporite formations, they require a part of aridity but also water, therefore rather a marked seasonality with a wet season. In addition, there are also evaporites linked to marine incursions.

We added description of the evaporite prediction scheme used in the model and explained the rationality of the comparison in section 5.1. Evaporites linked to marine incursions are excluded by kicking off those data points that are outside the land mask.

Lines 379- 386, 392-395.

Diagnosing the controls on desert dust emissions through the Phanerozoic

Yixuan Xie[1], Daniel J. Lunt[1], and Paul J. Valdes[1]

[1]School of Geographical Sciences, University of Bristol, Bristol BS8 1SS, UK

Correspondence: Yixuan Xie (yixuan.xie@bristol.ac.uk)

Abstract. Desert dust is a key component of the climate system, as it influences Earth's radiative balance and biogeochemical cycles. It is also influenced by multiple aspects of the climate system, such as surface winds, vegetation cover, and surface moisture. As such, geological records of dust deposition or dust sources are important paleoclimate indicators; for example, dust records can be used to decipher aridity changes over time. However, there are no comprehensive records of global dust variations on tectonic time scales (10's of millions of years). Furthermore, although some modelling studies have focused on particular time periods of Earth's history, there has also been very little modelling work on these long timescales. In this study, we establish for the first time a continuous model-derived timeseries of global dust emissions over the whole Phanerozoic (the last 540 million years). We develop and tune a new offline dust emission model, ~~DUSTY~~DUSTY1.0, driven by the climate model HadCM3L. Our results quantitatively reveal substantial fluctuations in dust emissions over the Phanerozoic, with high emissions in the Late Permian to Early Jurassic (×4 pre-industrial levels), and low emissions in the Devonian-Carboniferous (×0.1 pre-industrial levels). We diagnose the relative contributions from the various factors driving dust emissions and identify that the non-vegetated area plays a dominant role in dust emissions. The mechanisms of paleo hydrological variations, specifically the variations in low-precipitation-induced aridity, which primarily control the non-vegetated area, are then diagnosed. Our results show that paleogeography is the ultimate dominating forcing with the dust emissions variations explained by indices reflecting the land-to-sea distance of tropical and subtropical latitudes, whereas CO_2 plays a marginal role. We evaluate our simulations by comparing them with sediment records and find ~~fair~~ reasonable agreement. This study contributes a quantified and continuous dust emission reconstruction, as well as an understanding of the mechanisms driving paleohydroclimate and dust changes over Earth's Phanerozoic history.

1 Introduction

Dust plays a pivotal role in the Earth system. Dust affects the climate system in various ways. Dust modulates the Earth's radiation budget directly by scattering, absorbing and re-emitting radiation, but also indirectly regulates the Earth's radiation balance by stimulating cloud and precipitation formation processes (e.g. Schepanski, 2018). In addition, the deposition of dust onto the Earth's surface provides nutrients such as nitrogen, sulfur, iron and phosphorus, which affect the corresponding ecosystems and, ultimately, the global carbon cycle (Mahowald et al., 2017). For example, dust is the dominant external source of iron to the ocean, and the supply of iron is a limiting factor on marine life in large parts of the ocean and therefore influences the ability of the ocean to regulate atmospheric CO_2 (Jickells et al., 2005).

On the other hand, the climate system regulates dust processes in various ways. Rainfall, evapotranspiration, vegetation and the associated vegetation cover have an effect on sediment availability (Marx et al., 2018). Soil moisture, sediment particle characteristics, snow cover and surface wind jointly control the dust entrainment (Kok et al., 2012). In addition, shifts in wind regimes, such as the position of synoptic-scale circulation systems, and changes in clouds and precipitation at smaller-scale zones influence the transportation and deposition of dust (Marx et al., 2018).

The estimated global annual dust emission flux is about 2000 Mt, originating from the world's major deserts located in Africa, China and Mongolia, Australia, central and southwest Asia and the United States (Shao, 2001). The majority of the contemporary dust source regions are located in subtropical regions, which are associated with the position of the Hadley circulation: less . Less rainfall is produced in the mid-latitude extratropical latitudes Hadley Cell descending branch than its tropical ascending branch as a result of the meridional heat and energy transportation (Diaz and Bradley, 2004; Nguyen et al., 2013) (Diaz and Bradley, 2004; Nguyen et al., 2013), and hence lead leads to the broadly distributed subtropical aridity. In addition, the contribution of dust emissions from high-latitude paraglacial dust source regions is well constrained, accounting for about 5% of the overall dust budget (Bullard et al., 2016).

Because arid areas are in general associated with relatively high dust emissions, geological records of changes in dust emissions in Earth's past serve as a reliable archive for environmental and climate variations in aridity. In addition, past climates provide a natural laboratory for modelling studies which aim to explore controls on dust emissions.

Existing records of past dust emission/deposition show high variability through time. Reconstructions are most abundant in the Quaternary (the last 2.6 million years) and many of them indicate substantial glacial-interglacial variability – the Earth becomes dustier during glacial periods than interglacial periods (e.g. Lamy et al., 2014; Fitzsimmons et al., 2013) and records compiled in (Muhs, 2013) and (Kohfeld and Harrison, 2001)Muhs (2013) and Kohfeld and Harrison (2001). Studies have indicated that the more substantial glacial dust deposits could be attributed to increased wind intensities, a less vigorous hydrological cycle, decreased soil moisture, decreased vegetation cover, and exposed continental shelves (Winckler et al., 2008; Muhs, 2013), all of which are ultimately caused by variations in the Earth's orbital parameters. Some studies highlight the importance of glaciogenic dust as a significant sediment source due to glacial grinding (e.g. Mahowald et al., 2006; Sugden et al., 2009), which contributes to the formation of widespread loess deposits in the Quaternary (Li et al., 2020).

Similar orbital-driven dust (or aridity) records are also identified much further back in time, as early as such as during the Late Cretaceous (Niedermeyer et al., 2010; Vallé et al., 2017; Zhang et al., 2019) and at the late Paleozoic (Soreghan et al., 2008) . Moreover, the variability in dust (or aridity) on timescales older than the Quaternary is explained as responses to regional or global cooling (DeCelles et al., 2007; Bosboom et al., 2014; Licht et al., 2016; Zhang et al., 2016), atmospheric CO_2 concentration variations (Wang et al., 2023), tectonic movements (Rea et al., 1998; Licht et al., 2016; Farnsworth et al., 2019; Zhu et al., 2020; Anderson et al., 2020; Yang et al., 2021; Lin et al., 2024), or the absence of land vegetation (Liu et al., 2020), and intensified glaciation (McGlannan et al., 2022; Gabbott et al., 2010). However, these existing records and modelling studies have a relatively small scope, either spatially (only for a specific region) or temporally (only for a specific time period or a couple of time slices) or both, and there is also a lack of geological records of global dust variations through time. As such, our knowledge of the dust (or aridity) distributions, variations and the underlying driving forces in the Earth's deep time still remain insufficiently understood.

The aim of this study is, therefore, to investigate (1) How do the global dust emissions change through the Phanerozoic? (2) What are the causes and mechanisms of these changes? In order to do this, we develop a new offline dust emission model – ~~DUSTY~~DUSTY1.0, which is then driven by the output from a set of 109 General Circulation Model (GCM) simulations covering the whole Phanerozoic (last 540 million years).

The ~~DUSTY~~ DUSTY1.0 model and the underlying GCM and GCM simulations are described in section 2. The ~~DUSTY~~ DUSTY1.0 model is tuned to improve its simulations of the modern, described in Section 3. The paleo dust emissions simulations covering the whole Phanerozoic are then carried out with the tuned ~~DUSTY~~ DUSTY1.0 model. Results are shown in section 4, plus analyses of the contributing factors and the driving force of the Phanerozoic dust emissions variations. The credibility of our simulated dust emissions is evaluated with a comparison to geological records, with discussions of the implications and limitations of this study in section 5.

2 Methods

The following section describes the dust emission model "~~DUSTY~~DUSTY1.0" developed for this study, the GCM that is used to drive the ~~DUSTY~~ DUSTY1.0 model, and the simulations that have been carried out with the GCM.

2.1 The dust emission model "~~DUSTY~~DUSTY1.0"

The ~~DUSTY~~ DUSTY1.0 model developed for this study is an offline model. It is designed to be driven by dust-relevant ~~variables from any climatological field,~~ meteorological variables at a relatively high temporal frequency (for our study, every 1 hour), either the output from a GCM or observations, in order to calculate dust emissions for a particular climate scenario. Applying an offline dust model can make the dust simulation more efficient than using a coupled dust scheme within a GCM - allowing multiple sensitivity studies to be carried out without having to run the GCM multiple times. Also, for this study, due to the fact that we are simulating multiple time periods, we focus only on dust emissions rather than transport and deposition, in order to save computational cost. The dust emission model is designed to match the same spatial and temporal resolution of its driving input.

The following dust-relevant fields are used to drive the ~~DUSTY~~ DUSTY1.0 model: the land-sea distribution (l; equal to 0 or 1), the bare soil fraction of the land surface (b; varying from 0 to 1, non-vegetated area hereafter), the soil moisture (m; units ($kg\ m^{-2}$)), the snow cover (s; units ($kg\ m^{-2}$)) and the near-surface (~~10 meter~~ 10-meter height) wind velocity (u and v; zonal and meridional respectively, both units ($m\ s^{-1}$)). The spatial resolution of the dust model for this study is 96 × 73 grid points, which is 3.75° × 2.5° in longitude and latitude respectively, corresponding to the driving climate model (see Section 2.2).

The choice of the variables mentioned above is similar to other dust models. Vegetation and snow cover are commonly considered to inhibit dust emission from land surfaces and are generally represented in dust models with empirical ~~global~~

uniformed threshold values , globally uniform threshold values or as a linear function with no threshold (Ginoux et al., 2001; Miller et al., 2006; Kok et al., 2014). The formulation in our dust emission model assigns a linear function and a threshold for both (b_t and s_t respectively), which where the value is defined by further tuning process (Equations 3 and 5 below). Soil moisture is widely considered to suppress dust entrainment. Here we represent this with a simplified threshold-based (m_t) linear formulation (Equation 4 below), instead of considering it as a factor of threshold friction velocity of soil particles as in previous dust schemes (Pérez et al., 2011; Ginoux et al., 2001). As shown by many studies (e.g., Bagnold, 1941; Gillette and Stockton, 1989; Shao et al., 1993), dust emissions can be expressed in terms of surface wind speed above a threshold (U_{t1}), and the dust emission flux is approximately proportional to the third power of the wind speed. Our dust emission model adapts the formulation developed by (Gillette and Passi, 1988), Gillette and Passi (1988), which is also widely used in dust models such as (Tegen and Fung, 1994; Ginoux et al., 2001; Kerkweg et al., 2006; Miller et al., 2006; Chen et al., 2017) Tegen and Fung (1994); Ginoux et al. (2001); Kerkweg et al. (2006); Miller et al. (2006); Chen et al. (2017). We also add a maximum threshold (U_{t2}) for dust emissions to avoid spuriously large emissions when the surface wind speed is extremely strong (Equation 6). There are some factors omitted in this dust emission model compared to some existing dust schemes – the effect of particle size, their soil characteristics and mineralogical features that are believed to be factors for friction velocity of dust entrainment are not included in our dust emission model due to the absence of information on these aspects on the timescales we are addressing here. In addition, ‘"preferential sources areas’" (Zender et al., 2003; Cakmur et al., 2006) which are constrained by the surface topography as ’hydrological basins’, "hydrological basins", and the sediment availability related to the glacial grinding process (Prospero et al., 2002; Mahowald et al., 2006), are not considered in this dust emission model for the same reasons. As such, our model is supposed only to be able to test the hypothesis of dust emissions related to hydroclimate processes rather than the sediment supply hypothesis.

The total dust emissions index, d (no units) of each grid box, is the product of each individually ascribed emission index (Equation 1). d_l, d_b, d_m, d_s, d_U are corresponding emission indices associated solely with the land-sea distribution, the non-vegetated area, the soil moisture, the snow and the near-surface wind, as calculated by Equations 2 to 6 respectively.

$$d = d_l * d_b * d_m * d_s * d_U \tag{1}$$

$$d_l = l \tag{2}$$

$$d_b = \begin{cases} b, & \text{if } b > b_t \\ 0, & \text{otherwise} \end{cases} \tag{3}$$

$$d_m = \begin{cases} (m_t - m)/m_t, & \text{if } m < m_t \\ 0, & \text{otherwise} \end{cases} \tag{4}$$

$$d_s = \begin{cases} (s_t - s)/s_t, & \text{if } s < s_t \\ 0, & \text{otherwise} \end{cases} \tag{5}$$

$$U = \sqrt{u^2 + v^2}, \qquad d_U = \begin{cases} 0, & \text{if } U < U_{t1} \\ (U - U_{t1}) * U^2, & \text{if } U_{t1} \leq U \leq U_{t2} \\ (U_{t2} - U_{t1}) * U_{t2}^2, & \text{if } U > U_{t2} \end{cases} \tag{6}$$

Specifically, the land-sea distribution gives the basis for subsequent calculations as all the dust emissions are only considered over land areas. The calculation of consequent dust emissions related to bare soil, soil moisture and snow cover are all threshold-based linear relational expressions. The corresponding index for dust emissions induced by surface winds is calculated as a cubic relationship with two thresholds.

$$D = C_2 * d \tag{7}$$

A coefficient C_2 is here used to calibrate the total dust ~~emissions~~emission for the specific grid box, D (Equation 7), and to convert to units of kg m^2 s^{-1}. A globally averaged emission rate of $1.96 * 10^{-10}$ $kg\ m^{-2} s^{-1}$ is used (see details in section 3.1) to derive the coefficient C_2. This coefficient and the following coefficients introduced in the next paragraph are all calculated at a global mean level.

In addition, The dust emission model also produces dust emissions with various combinations of those dust-relevant fields, either included or not included. Using the same naming convention as in equation 7, the emissions calculated are D^l, D^{lb}, D^{lbm}, D^{lbms}, D^{lbU}, D^{lbmU}, D^{lbsU}, as given in equation 8. Similar to C_2, different coefficients (C_1, C_3, C_4, C_5) are used in order to scale the emissions with various process combinations. C_1 is chosen such that the global dust emissions in D^{lbms} are equal to D^{lbmsU}, C_3, C_4, C_5 are chosen such that the global dust emissions in D^{lbU}, D^{lbmU} and D^{lbsU} are equal to D^{lbms}.

$$\begin{aligned} D^l &= C_1 * d_l \\ D^{lb} &= C_1 * d_l * d_b \\ D^{lbm} &= C_1 * d_l * d_b * d_m \\ D^{lbms} &= C_1 * d_l * d_b * d_m * d_s \\ D^{lbU} &= C_3 * d_l * d_b * d_U \\ D^{lbmU} &= C_4 * d_l * d_b * d_m * d_U \\ D^{lbsU} &= C_5 * d_l * d_b * d_s * d_U \end{aligned} \tag{8}$$

2.2 The GCM

For this study, the ~~DUSTY~~ DUSTY1.0 model is driven by simulations carried out with a General Circulation Model (GCM) HadCM3BL-MOSES2.1a-TRIFFID (HadCM3BL-M2.1aD in the naming convention of Valdes et al. (2017); henceforth HadCM3L). This is a coupled atmosphere-ocean-vegetation model. The atmospheric component of HadCM3L solves the primitive equation set of White and Bromley (1995) through the Arakawa staggered B-grid scheme from Arakawa and Lamb (1977). Parameterisations include the convection scheme of Gregory et al. (1997), the large-scale precipitation scheme of Wilson (1998), the radiation scheme of Edwards and Slingo (1996), and the clouds scheme of Bushell (1998). The ocean component is based on the model of Cox et al. (1984), which is a three-dimensional ocean model. Parameterisations include the ocean mixed layer schemes of Turner and Kraus (1967). Modifications to the ocean vertical diffusion and isopycnal diffusion due to the model's lower resolution are described in detail in Valdes et al. (2017). There are also modifications in the bathymetry of the North Atlantic, which improves the reality of heat transports in the coupled system and alleviates the need for flux correction and makes the model more appropriate for paleo simulations.

The land surface scheme MOSES2.1 calculates the energy and moisture between the land surface and the atmosphere and updates the relevant surface and subsurface variables (Cox et al., 1999). It is coupled with an interactive vegetation model, TRIFFID, via nine land cover types: broadleaf trees, needleleaf trees, shrubs, C3 grasses, C4 grasses, urban, inland water, bare soil and land ice. TRIFFID takes the averaged flux of carbon from MOSES2.1, calculates the growth and expansion of five defined plant functional types and updates the vegetation fractions and parameters through competitive, hierarchical formulation. We do not change this representation of vegetation, even though grasses did not become dominant until after the end-Cretaceous, and C4 vegetation did not become dominant until much later. Our assumption is that other forms of ground cover vegetation were present in these older time periods and impacted climate in similar ways.

HadCM3L has a horizontal resolution of 96 × 73 grid points in both the atmosphere and the ocean, which is 3.75º × 2.5º in longitude and latitude, and 19 hybrid vertical levels in the atmosphere and 20 vertical levels in the ocean with finer definition closer to the surface. It is of relatively lower resolution compared to recent state-of-the-art CMIP6 models, therefore, it is particularly computationally efficient and applicable for multi-million-year scale simulations. The model has been used widely in pre-Quaternary climate modelling studies (e.g. Marzocchi et al., 2015; Wade et al., 2019; Jones et al., 2022).

Since Valdes et al. (2017), the model has undergone several improvements, the most significant of these is a tuning process designed in particular to improve the deep-time climate simulations. The changes made follow those described in Sagoo et al. (2013); Kiehl and Shields (2013), primarily targetting parameters associated with clouds; this results in a flatter meridional temperature gradient in warm climates, which is in better agreement with paleoclimate proxies. ~~More details of this process are described in ?.~~ In addition, we have added a new representation of soil albedo. In the original model configuration, soil was specified as a medium loam everywhere. We have now added a soil carbon dependence. If the soil carbon content drops below 15 $kg\,m^{-2}$, the albedo linearly increases to a maximum of 0.355. These numbers were tuned so that the model could simulate the present-day average Saharan soil albedo well.

2.3 The GCM simulations

This study uses 3 series of 109 experiments each, S_1, S_{1noCO2} and S_2, all carried out with HadCM3L, corresponding to roughly 109 geological stages covering the whole Phanerozoic (since 541 million years). Similar simulations are described in Valdes et al. (2021). However, the Valdes et al. (2021) simulations do not include the tuning processes described in section 2.2. Series S_2 does include those tuning, but is otherwise identical to series S_1. The boundary conditions to drive the S_1 and S_2 simulations include (1) solar constant following ~~(Gough, 1981)~~Gough (1981); (2) atmospheric CO_2 concentrations following ~~(Foster et al., 2017)~~Foster et al. (2017); and (3) paleogeography (the configuration and height/depth of the continents and oceans) following ~~(Scotese and Wright, 2018)~~Scotese and Wright (2018). The boundary conditions used to drive S_{1noCO2} are identical ~~,~~ to those described above in terms of solar constants and paleogeography but with a fixed atmospheric CO_2 concentration at pre-industrial levels (276.01 ppm). These simulations have been run for an additional 3000 years beyond those described in ~~(Valdes et al., 2021)~~Valdes et al. (2021). To conduct this dust study, each of the 109 experiments is also run for an additional 30 years with the dust-relevant variables (m, s, u, v) output at an hourly resolution.

The "0 Ma simulation" (the latest of the 109 simulations, corresponding to the pre-industrial configuration) is designed to be consistent with the rest of the paleo simulations in terms of most of the boundary conditions, for example, having homogeneous soil properties. As such, it is not the most accurate possible simulation of the pre-industrial climate. In order to tune the dust model with the pre-industrial scenario, we therefore also carry out another "standard pre-industrial simulation" with HadCM3L, which has more realistic pre-industrial boundary conditions. The main differences between them are – (1) the vegetation in the standard pre-industrial simulation is from observations, whereas the vegetation in the 0 Ma simulation is calculated by the coupled vegetation scheme; (2) the topography of the standard pre-industrial simulation is from observation, whereas the topography of the 0 Ma simulation is from the ~~(Scotese, 2016)~~ Scotese (2016) reconstructions; (3) the surface variables, primarily soil properties, are globally homogeneous in the 0 Ma simulation but are spatially varied based on observations in the standard pre-industrial simulation.

3 Dust model tuning

Given that there are uncertainties in the "correct" values of the thresholds b_t, m_t, s_t, U_{t1}, U_{t2} and the coefficients C_1, C_2 etc., it is necessary to design a tuning process to identify the values that give the most realistic results for D. The assumption is that the tuning is carried out for the pre-industrial simulation, and the same tuned variables are assumed to be appropriate for all the paleo simulations.

3.1 Methods of tuning

In order to calibrate the dust model, a target needs to be selected as a benchmark. Theoretically, the target that the model is tuned to should be based on observations. In practice, the parameters commonly provided by modern dust observations are Dust Optical Depth or Aerosol Optical Depth (e.g. Gkikas et al., 2021), which are properties primarily influenced by the

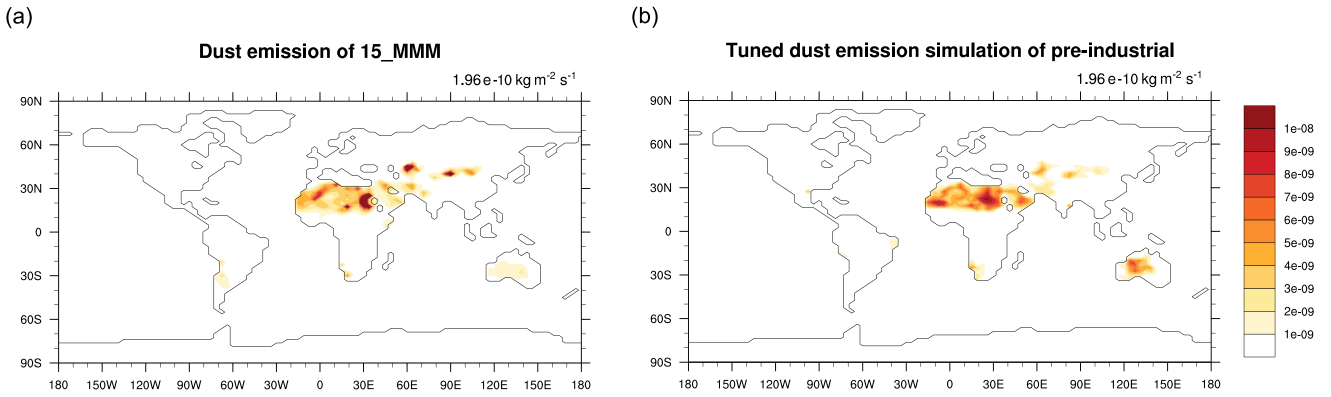

Figure 1. The pre-industrial dust emissions fields **(a)** averaged from the 15 CMIP6 AMIP models, which is used in this study as the tuning target, **(b)** simulated from the tuned ~~DUSTY~~ DUSTY1.0 model (plot from model version one; see details about model versions in section 3.2 and Table 1). Both values at the top-right are the global mean dust emission rates.

suspended dust particles in the atmosphere, whereas our dust model only predicts the surface emissions. Therefore, we use simulated modern dust emissions from other (more complex) coupled climate-dust models as the tuning target. Here we use the multi-model mean of 15 CMIP6 AMIP models (hereafter 15_MMM, Figure 1a) which is the dust emission over the period 2005-2014. In the absence of dust emissions from observations, this is justified partly by the complexity and resolution of CMIP6 models being higher than HadCM3L, which are therefore expected to predict more accurate dust emissions than the dust model in this study; and partly because the mean of several models in general has a lower bias than the output of a single model, and therefore represents a valid tuning target. The dust particle size range varies among the 15 models, with the smallest size bin of 0.064-0.2 μ (HadGEM3-GC31-LL) and the largest with a diameter of 20-63 μ (HadGEM3-GC31-LL and UKESM1-0-LL) (Zhao et al., 2022). This also limits the range of particle sizes that DUSTY1.0 can effectively cover. The global average dust emission rate given by the 15_MMM is $1.96 * 10^{-10}\ kg\ m^{-2} s^{-1}$, which is used to calculate the ~~C_1~~ C_2 in equation (7) in each tuning experiment, so that the standard pre-industrial dust simulation has an identical global mean dust emission rate as the target. Every global mean value is calculated over all the grid boxes rather than over all the land grids to avoid confusion arising from variations in the total land area over time.

In addition to scaling the global average dust emission rate to the target, the main aim of the model tuning process is to find the optimum choices of the threshold values of the dust model that give the best fit to the spatial pattern of the target. When evaluating the model, it is necessary to use a cost function to quantitatively measure the difference between the simulations and the target. The metric chosen here is the “Arcsin Mielke” score (AMS, Watterson et al. (2014)). For a modelled dust field D, and an observed dust field T, the AMS is defined as

$$AMS = \frac{2000}{\pi} arcsin[1 - mse/(V_D + V_T + (G_D - G_T)^2)] \quad (9)$$

where mse is the mean-square error between T and D, V_D and V_T are the spatial variances of D and T respectively, G_D and G_T are the spatial means of D and T respectively. The AMS has a maximum possible value of 1,000, where the modelled result is identical to the target.

To perform the tuning, a Latin Hypercube Sampling (LHS, Mckay et al. (1979)) method is used. LHS is a stratified-random procedure which provides an efficient way of sampling variables. In this study, the number of samples, which is also the number of tested model versions, is 200. This decision is a trade-off between having as many samples as possible and the cost of computing time. The five-dimensional parameter space where the 200 samples are taken from, is constrained by the range of b_t, m_t, s_t, U_{t1} and U_{t2}. We take a two-step approach here. Firstly, the initial range for each threshold is derived from the variable's distribution in the standard pre-industrial GCM simulation, or based on previous studies. Specifically, the bare soil values of the preindustrial simulations vary from 0 to 1, so the initial test range is set to be the [0.0-1.0]. The soil moisture at the southern edge of the Sahara area, where modern dust emissions are relatively low, is around 20.0 to 24.0 ($kg\ m^{-2}$), so the initial test range is set at a slightly wider range of 18 to 28 ($kg\ m^{-2}$). For snow cover, ~~(Lunt and Valdes, 2002)~~ Lunt and Valdes (2002) apply a snow cover threshold in their dust model of 20.0 $kg\ m^{-2}$; as such the initial test range of 15.0 to 25.0 ($kg\ m^{-2}$) is chosen to encompass that value. The global minimum wind speed is around 0.8 $m\ s^{-1}$ and the maximum wind speed over land does not exceed 6.0 $m\ s^{-1}$, as such, a reasonable initial test range of U_{t1} is set as 0.8 to 4.0 ($m\ s^{-1}$), and 4.0 to 6.0 ($m\ s^{-1}$) for U_{t2}. Secondly, starting from the initial test ranges described above, further adjusting (expanding, shrinking or shifting) to the test range has been carried out in an iterative process, with the aim of identifying appropriate ranges for the 200 sampled experiments. The final ranges applied are 0.2 to 0.34 for bare soil, 16.0 to 30.0 ($kg\ m^{-2}$) for soil moisture, 14.0 to 50.0 ($kg\ m^{-2}$) for snow cover, 0.2 to 2.0 ($m\ s^{-1}$) for U_{t1} and 2.0 to 5.5 ($m\ s^{-1}$) for U_{t2}, as shown in Figure 2.

3.2 Tuning results

The results of the tuning exercise are shown in Figure 2. As a post hoc justification of the parameter ranges identified in Section 3.1, the results of the tuning show that the relatively high AMS values (i.e. the best fitting parameters) are not situated close to the edges of the ranges.

We select the dust emission model versions with the top five AMS results from the tuning exercise (as shown in black dots in Figure 2). The corresponding thresholds and coefficients are listed in Table 1. The tuned standard pre-industrial dust emission simulation (simulated from tuned parameter set version 1, all maps shown hereafter are results from model version 1 as a representative) is shown in Figure 1b. The tuned simulation generally captures the spatial pattern of global dust emission regions as defined by the 15_MMM, with northern Africa and central Australia predominating, followed by central ~~Asia~~Eurasia, and minor regions in South Africa. There are also many discrepancies exist between the tuned simulation and the target; for example, the high emissions hot spots in the Eastern Sahara and central Eurasia (Figure 1a) are not found in the stunned simulation (Figure 1b), while the tunned simulation gives higher emissions in the board Australia desert area. This discrepancy is largely due to the absence of detailed morphology and particle size representation in our models. These factors are crucial for capturing small-scale areas with frequent dust activation. Because we force the DUSTY1.0 model to match the global

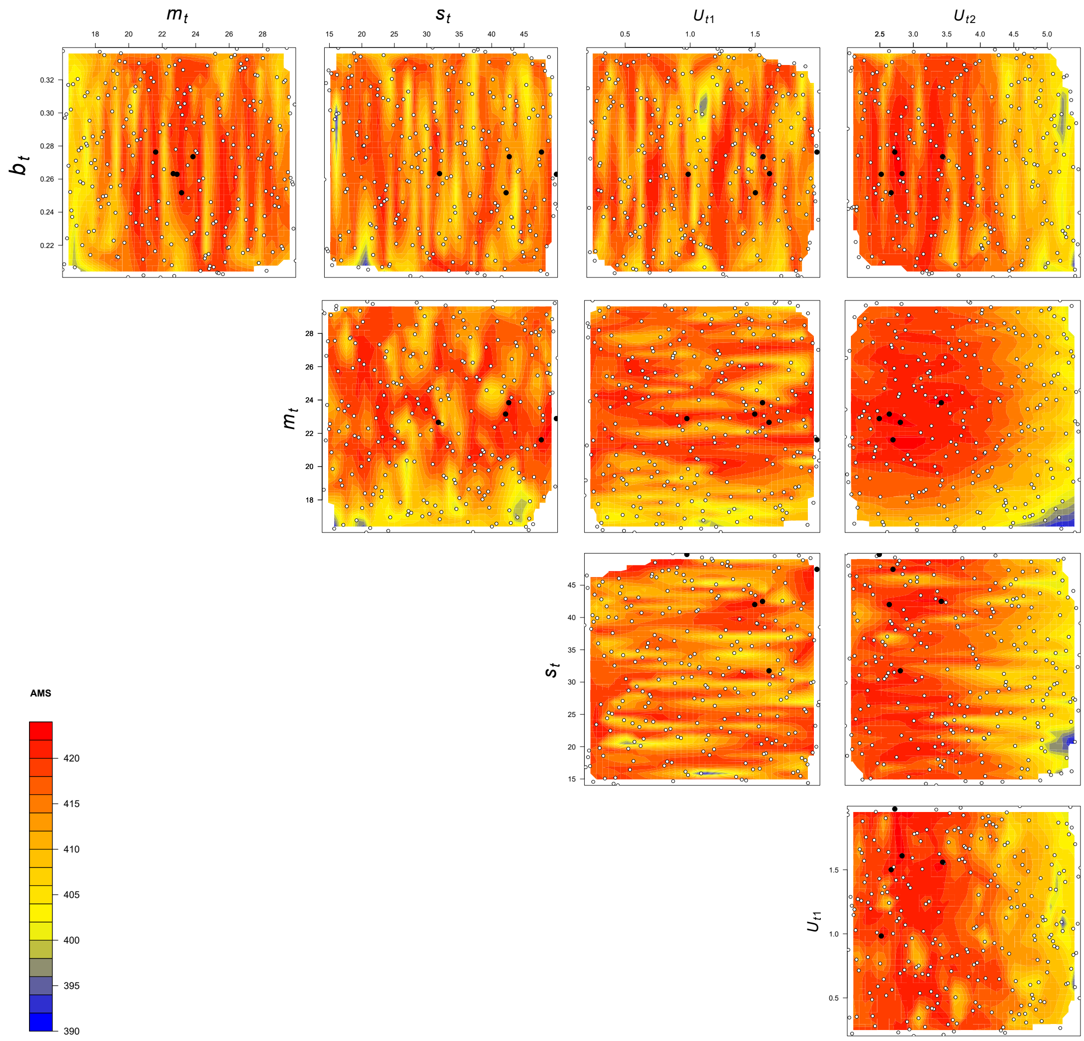

Figure 2. The performance of 200 dust emission model versions with different thresholds, measured by their AMS, compared to the tuning target. The ranges for each threshold shown in this figure are all final ranges, Each panel has 200 dots representing all the samples taken within the corresponding ranges, where the five solid dots are the top-ranked ones.

mean emission rate of the target, the average emission in each sub-area is enhanced in the absence of hot spots, which leads to overestimation in regions like Australia and western Sahara.

Table 1. Summary of thresholds valued applied in the top five ~~DUSTY~~ DUSTY1.0 model versions

Tuned ~~DUSTY~~ model version number	~~C_1~~ C_2	b_t	m_t	s_t	U_{t1}	U_{t2}
1	1.88e-08	0.26	22.66	31.75	1.61	2.83
2	2.11e-08	0.28	21.61	47.45	1.97	2.72
3	1.69e-08	0.27	23.84	42.49	1.56	3.44
4	1.78e-08	0.25	23.16	42.00	1.50	2.67
5	1.83e-08	0.26	22.88	49.76	0.98	2.52

4 Phanerozoic dust emissions and controls

This section presents the paleo application of the dust model, including the simulated dust emissions over the Phanerozoic (Section 4.1), analysis of the contributions from the factors (Section 4.2), and the evolution of aridity in response to paleogeography (Section ~~??~~4.3).

4.1 Dust emissions over the Phanerozoic

The five tuned versions of the dust emission model in section 3.2 are applied to all 109 ~~time slices~~ simulations from series S_2 (see details in section 2.3 through the Phanerozoic (since 540 Ma). Here we show the simulated global averaged dust emission rate time series in Figure 3, and the simulated dust emission fields for five example time slices (0 Ma, 196Ma, 252Ma, 370Ma, and 530 Ma) in Figure 4 (the dust emission field for all 109 experiments can be found in Appendix in Figure A2-A5). Most notably, the dust emissions are significantly high during the period over the late Permian to the early Jurassic (263 Ma to 191 Ma), where there are two peaks, one covering the Permian-Triassic transition (252 Ma) at the emission rate of $9.1*10^{-10}\ kg\ m^{-2}s^{-1}$ and the other spanning the middle Triassic to the early Jurassic (196 Ma) at the emission rate of $8.5*10^{-10}\ kg\ m^{-2}s^{-1}$. The emission rates for both peaks are more than four times the pre-industrial level ($1.96*10^{-10}\ kg\ m^{-2}s^{-1}$). The dust provenance areas for both peaks are concentrated in the central supercontinent, covering the mid-latitudes, subtropics, and the tropics, as illustrated in Figure 4~~bc~~b and c. The global dust emission rate reaches its lowest in the Devonian-Carboniferous transition (366 Ma) at the level of $1.9*10^{-11}\ kg\ m^{-2}s^{-1}$, which is almost ten times less than the pre-industrial level. Dust provenance areas are scattered throughout the mid-latitudes in both hemispheres (Figure 4d) at that time. In the early Cambrian (541 Ma to 535 Ma), the oldest simulation we carry out, dust emission rates ($1.6*10^{-10}\ kg\ m^{-2}s^{-1}$) are close to the pre-industrial level, and the dust source regions are centred in the mid-latitudes of both hemispheres (Figure 4e). Evaluations ~~on~~ of the simulated dust emission in comparison to geological records will be discussed in section 5.1. Similar to the discrepancy mentioned in section 3.2, our paleo simulations may not be able to represent high-emission hot spots and, alternatively, may overestimate emission rates in broadly-distributed but low-emission-rate desert areas. Further uncertainties arising from the GCM simulating vegetation in the absence of land plants during the early Paleozoic will be discussed in section 5.2.

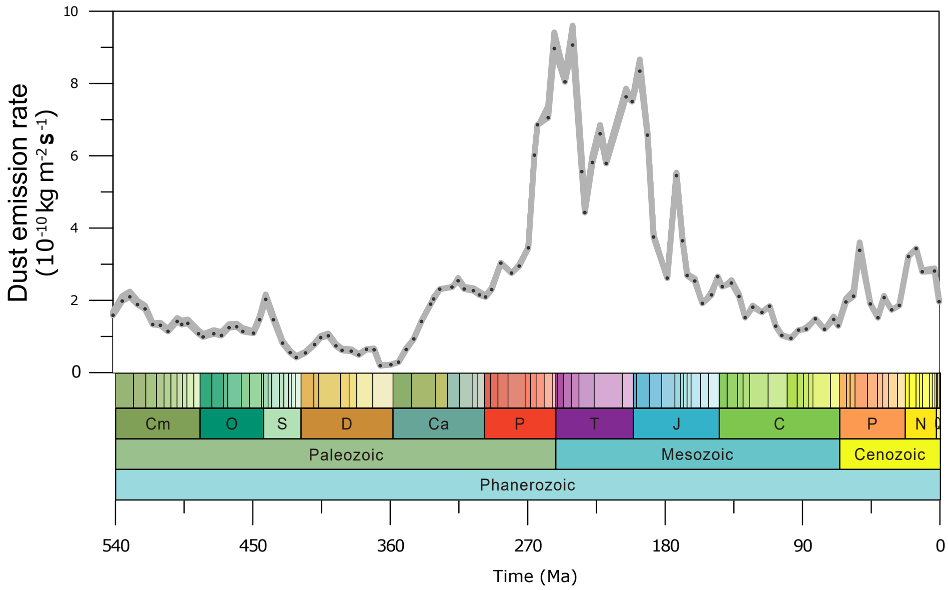

Figure 3. Time series of the simulated global average dust emission rate over the Phanerozoic. The grey shading (not a curve) in the figure is a stack of the results from those five top-ranked model versions, and the dots on it represent the results of model version one to hint at the time intervals between simulations of different time slices.

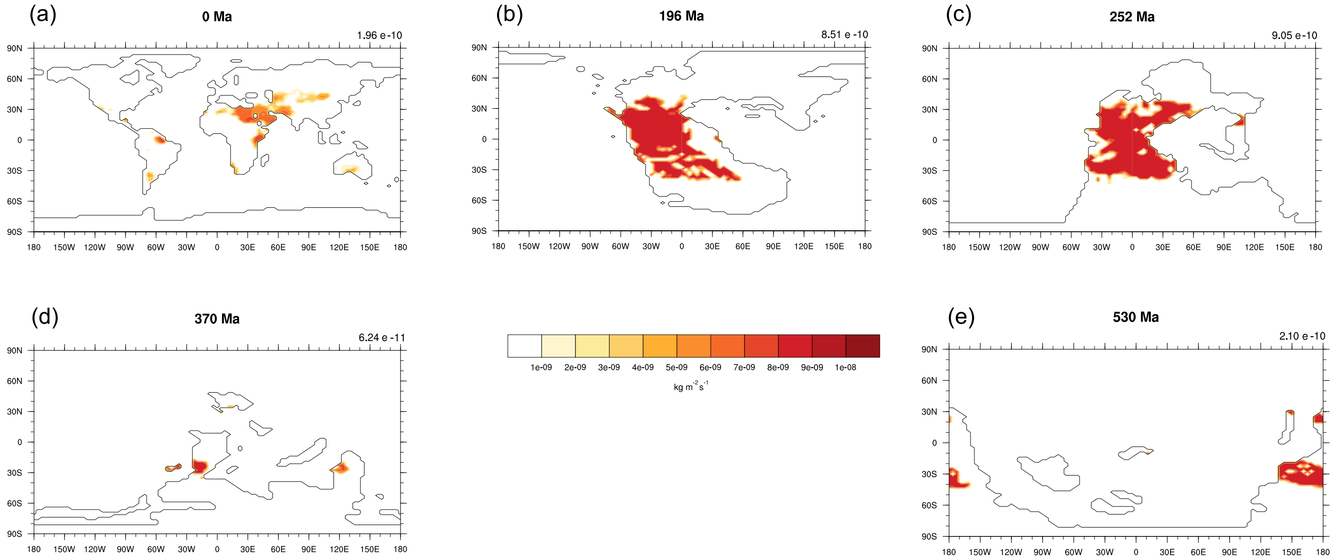

Figure 4. A few examples of the simulated dust emissions. The examples are for **(a)** present day (0 Ma), **(b)** the early Jurassic (196 Ma), **(c)** the early Triassic (252 Ma), **(d)** the late Devonian (370 Ma), and **(e)** the early Cambrian (530 Ma). Values at the top-right of each panel are the corresponding global mean dust emission rate. All unites are $kg\, m^{-2} s^{-1}$.

4.2 Contributing factors to the dust emissions

The simulated dust emissions described in section 4.1 show substantial fluctuations over the Phanerozoic. In order to understand the causes of the fluctuations, we here use a factorisation approach to analyze and quantify the relative importance of each variable (the land-sea distribution l, the non-vegetated area b, the soil moisture m, the snow cover s and the near-surface wind U, all introduced in section 2.1) that is used to drive the dust emission model.

The factorisation is carried out in a two-step approach, where the analysis of l and b is performed as a linear factorisation, whereas the analysis of m, s and U is performed based on the 'linear sum' factorisation method according to (Lunt et al., 2021), which is suitable for diagnosing a multi-variate system. We understand the whole system from a starting point in which there are no dust emissions anywhere on the globe, D^0. We then add the factors l and b sequentially, to produce D^l and D^{lb} respectively (the linear factorisation). We then carry out an unordered addition of the three remaining factors m, s, and U, producing D^{lbm}, D^{lbs}, D^{lbU}, D^{lbms}, D^{lbmU}, D^{lbsU} and D^{lbmsU} (see Section 2.1 for the naming convention). Details of the factorisation are described in the appendix with the factorisation concept illustrated in Figure A1. The contributions of each factor are quantified for the land-sea distribution, vegetation, soil moisture, snow cover, and wind, as ΔD^l for the land sea distribution, ΔD^b,ΔD^m,ΔD^s, and ΔD^U, respectively.

The factorisation is applied to all the time slices to quantify the contribution of each factor and how this varies over time, as illustrated in Figure 5. The contribution from the land-sea distribution factor (ΔD^l = D^l, brown line in Figure 5a) results in dust emissions of about 3.5 kg/m^2 over the early Phanerozoic, increasing to a maximum around 250 Ma, and then decreasing to about 90 Ma before increasing slightly to the modern. Following is the contribution from the non-vegetated area factor (ΔD^b), which reduces the dust emissions remarkably over time. ~~Regarding the reality that~~ As expected, the non-vegetated area and land-sea distributions are ~~inalienable,~~ very important, and the joint contribution from both l and b (ΔD^{lb}) gives a more concrete reflection ~~, which is~~ of this. It shows that they are three times the all-forcing dust emissions (D^{lbmsU}). The addition of m and s both reduce the dust emission. The contribution from m (ΔD^m) is approximately double the all-forcing dust emissions, whereas the contribution from s (ΔD^s) is only 1% of the all-forcing dust emissions. The addition of U alters dust emissions most positively over time but also has adverse effects for a few time periods in the mid-Permian, early-Cretaceous and late-Paleogene. It contributes an average of 44% of the all-forcing dust emissions before the Carboniferous and 27% of the all-forcing dust emissions during the late Permian to the early Jurassic.

The analysis above quantifies the magnitude of each factor to the total global dust emissions for each time slice individually. A complementary approach is to quantify the impact of each factor on the temporal variability of emissions throughout time, i.e., the extent to which the shape of the emission timeseries improves towards the all-forcing emission timeseries as the result of the inclusion of a specific variable. In order to evaluate this, for each combination of factors, we calculate the correlation coefficient of the resulting emissions timeseries with the all-forcing emissions timeseries. We then drive the contribution from the difference in these correlation coefficients, The greatest contribution to the temporal variability in emissions is made by l (66.53%), followed by b (31.86%), U (1.22%), m (0.34%), and finally s (0.05%).

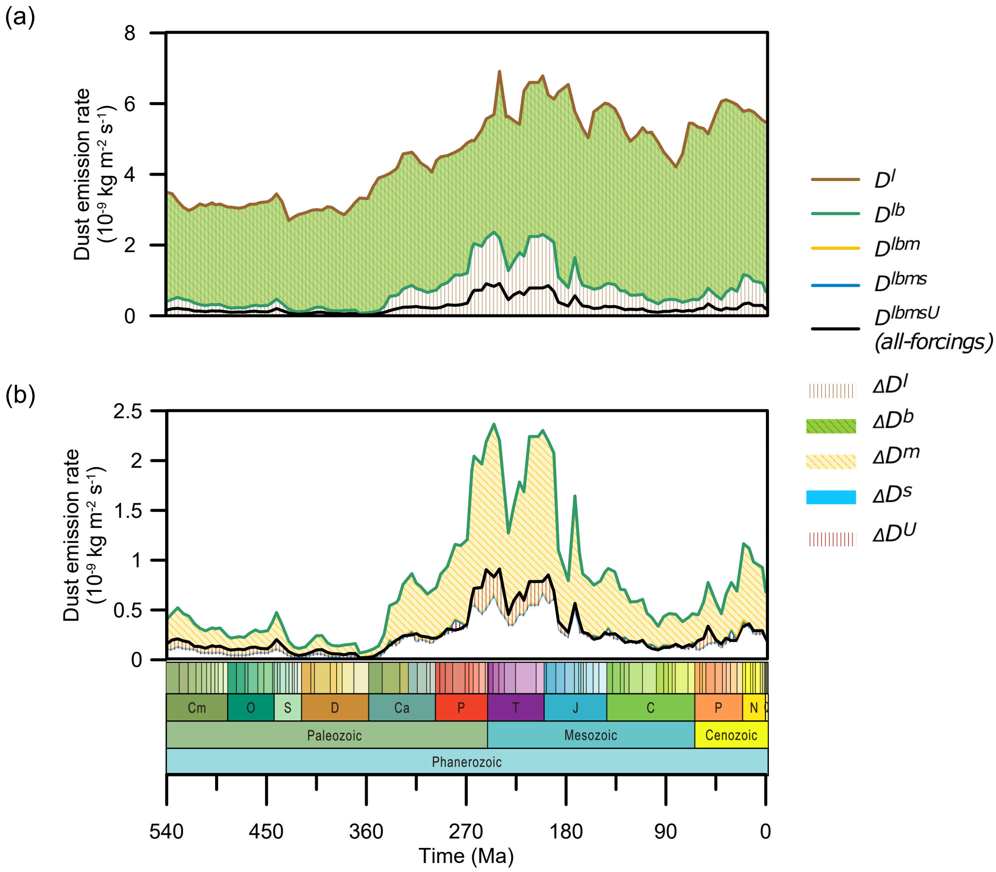

Figure 5. The decomposed contribution of individual factors to the total dust emissions over the Phanerozoic. **(a)** Results for l and b,**(b)** Results for m, s and U. Note that the ranges of y-axes differ between panel **(a)** and **(b)**. All curves refer to the joint dust emissions derived from the corresponding superscript variables, and the shadings refer to the dust emissions contributed from each specific superscript variable. (e.g. D^{lb} refers to the simulated dust emissions when only variables l and b are included in the ~~DUSTY~~ DUSTY1.0 model, and ΔD^m refers to the quantified dust emissions contribution of the sole variable m)

4.3 The paleogeographical control on the desert area

As shown in Section 4.2, the combined land and non-vegetated area factors (D^{lb}) dominate the dust emission variations on geological timescales. Given that the non-vegetated area changes implicitly also include the land area changes (i.e. D^b=D^{lb}), here we focus on the mechanisms for the changes in non-vegetated areas.

We here measure the extent of aridity with an aridity index (AI) that is threshold-based and inversely proportional to the amount of precipitation:

$$AI = (t_{arid} - precipitation)/t_{arid}), \tag{10}$$

where t_{arid} is set as 0.8 mm/day. This threshold is selected because sediments such as evaporite and weathered sandstone, which are indicators of arid environments, are formed under a limit of approximately 0.8 mm/day (Cecil, 2003; Warren, 2010; Price et al., 1 .

The non-vegetated fraction in the simulations are very closely controlled by the precipitation rate. In particular, the area of precipitation that is less than 0.8 mm/day (represented by the Aridity Index) shows a very strong positive linear relationship with the non-vegetated area (Figure 6ab, correlation coefficient = 0.98). And as we have shown above, the non-vegetated fraction controls the total dust emissions. In addition to the global means, the zonal mean distribution of continental precipitation varies over time (Figure 7c), as does the zonal mean Aridity Index (Figure 7d. The aridity index shows a very similar pattern to the dust emissions (Figure 7e). As such, the continental distribution, combined with the zonal mean precipitation (Figure 7ab) are sufficient to closely approximate the dust emissions (Figure 7e).

The challenge then becomes to understand the controls on zonal mean precipitation (Figure 7a). There are three boundary conditions that are changing over time which must ultimately control the precipitation changes; namely, CO_2, solar constant, and paleogeography. Firstly, in order to explore the impact of CO_2 change, here we take the results from an additional series of GCM simulations, as a sensitivity test. Comparison of results from the S_1 and S_{1noCO2} simulations (described in section 2.3) reveal the negligible effect of CO_2 concentration on the precipitation low precipitation area variation over time (Figure 8b), and therefore aridity (Figure 8a). Hence, we conclude that on these timescales, CO_2 is not a strong control of the aridity. Furthermore, the change in solar constant through the Phanerozoic is linear, whereas the dust emissions change is highly non-linear. As such, we can attribute the mechanism of changes in precipitation, aridity, and ultimately dust emissions, to the only remaining boundary condition change, namely paleogeography.

(a) Comparison of low precipitation area fraction time series from three different experimental series: S_1, S_1noco2 and S_2. A daily mean precipitation of less than 0.8 mm is considered low precipitation. **(b)** Comparison of zonal mean land precipitation over the Phanerozoic between experimental series S_1 and S_1noco2.

In general, it may be expected that regions in the continental interiors are more arid due to being remote to oceanic moisture sources. Here we develop indices measuring the distance of the shortest pathway from land to ocean. The distance indices are calculated in the tropical zone (23.5°N to 23.5°S, TD), the subtropical zones in the Northern Hemisphere (35°N to 23.5°N,$NSTD$) and the subtropical zones in the Southern Hemisphere (23.5 °S to 35°S, $SSTD$) respectively, as shown in Figure 6c. During the period prior to the Carboniferous, the global aridity (Figure 6b) shows a remarkably similar temporal evolution to TD and $SSTD$, which drop remarkably in the Silurian and Devonian. Since the Carboniferous, more continents shift to the tropics and the Northern Hemisphere, and the overall growth of global aridity is therefore driven by the combined effect of TD and $NSTD$ until the late Permian (excepting a short drop-down at the late Carboniferous when the $SSTD$ exerts a control). The extreme aridity from the late Permian to the late Triassic is controlled by all three land-sea distance indices, which is due to the fact that the supercontinent covers almost all latitudes during the corresponding times. The extreme aridity can be divided into two peaks during this period. The first aridity extreme at the Permian-Triassic boundary is mainly driven by the $SSTD$, the second aridity extreme at the late Triassic is mainly driven by the TD, while the $NSTD$ contributes equally to both. The land-sea distance indices have decreased in all three latitude zones since the early Jurassic due to continuous continent convergence, resulting in overall humidification until the Cretaceous-Paleocene boundary, where the decrease of $SSTD$ plays a relatively significant role. It is important to note that there are other factors contributing to this widespread aridity, which corresponds to the collapse of the tropical land humid zones as shown in Figure 7c. With the latest improvement in vegetation albedo parameterization in the GCM (see description in section 2.2), the low vegetation coverage will trigger a positive feedback loop where higher surface albedo leads to lower net solar radiation and an increase in radiative cooling. This then suppresses convection and leads to amplification and potential expansion of the dry conditions (Charney et al., 1977) . From the Cenozoic onward, the continents have shifted further northward, resulting in the $NSTD$ being the dominant control of the expanding aridity. Overall, these distance indices are able to approximately explain the change in global mean aridity over time.

As the

Overall, as the fundamental driving factor, paleogeography controls the geological timescale aridity and, thus, dessert desert area variations over the Phanerozoic.The dust source area desert dust is consistently found in subtropical land areas of either hemisphere over time , resulting from a relatively constant meridional atmospheric circulation pattern throughout the Phanerozoic. Under this fairly fixed meridional precipitation pattern, it is the drifting and converging of continental land that truly determines the location of desert regions and the amount of dust emissionsand also in the tropical during supercontinent times. These can be mainly explained by variations in the land-to-sea distance. To some extent, the higher albedo over sparesely vegetated areas further amplifies the spreading of aridity into the tropics during supercontinent times.

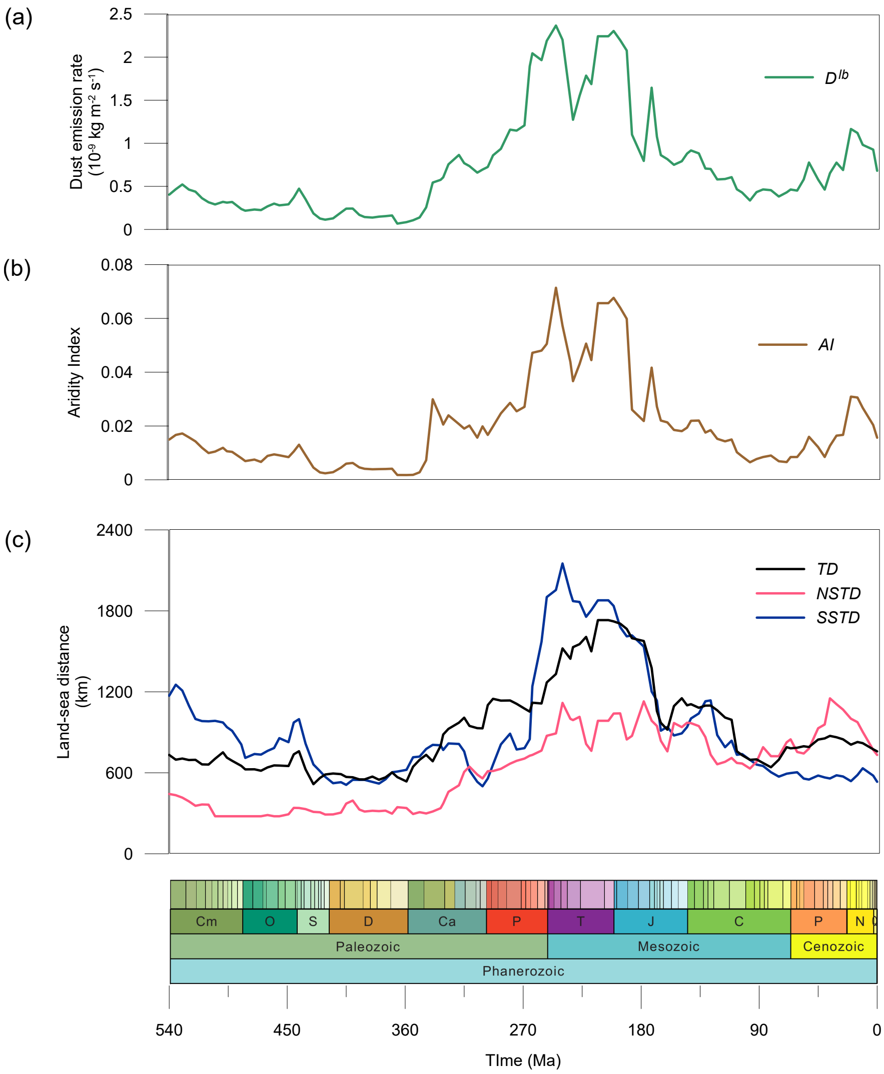

Figure 6. Time series of **(a)** D^{lb}, which is the simulated global average dust emissions jointly contributed from l and b, **(b)** the AI (aridity index), which reflects the lowness of precipitation, and **(c)** the land-sea distance indices, in which TD refers to the tropics, $NSTD$ and $SSTD$ corresponds to the subtropics of the Northern and Southern Hemispheres, respectively.

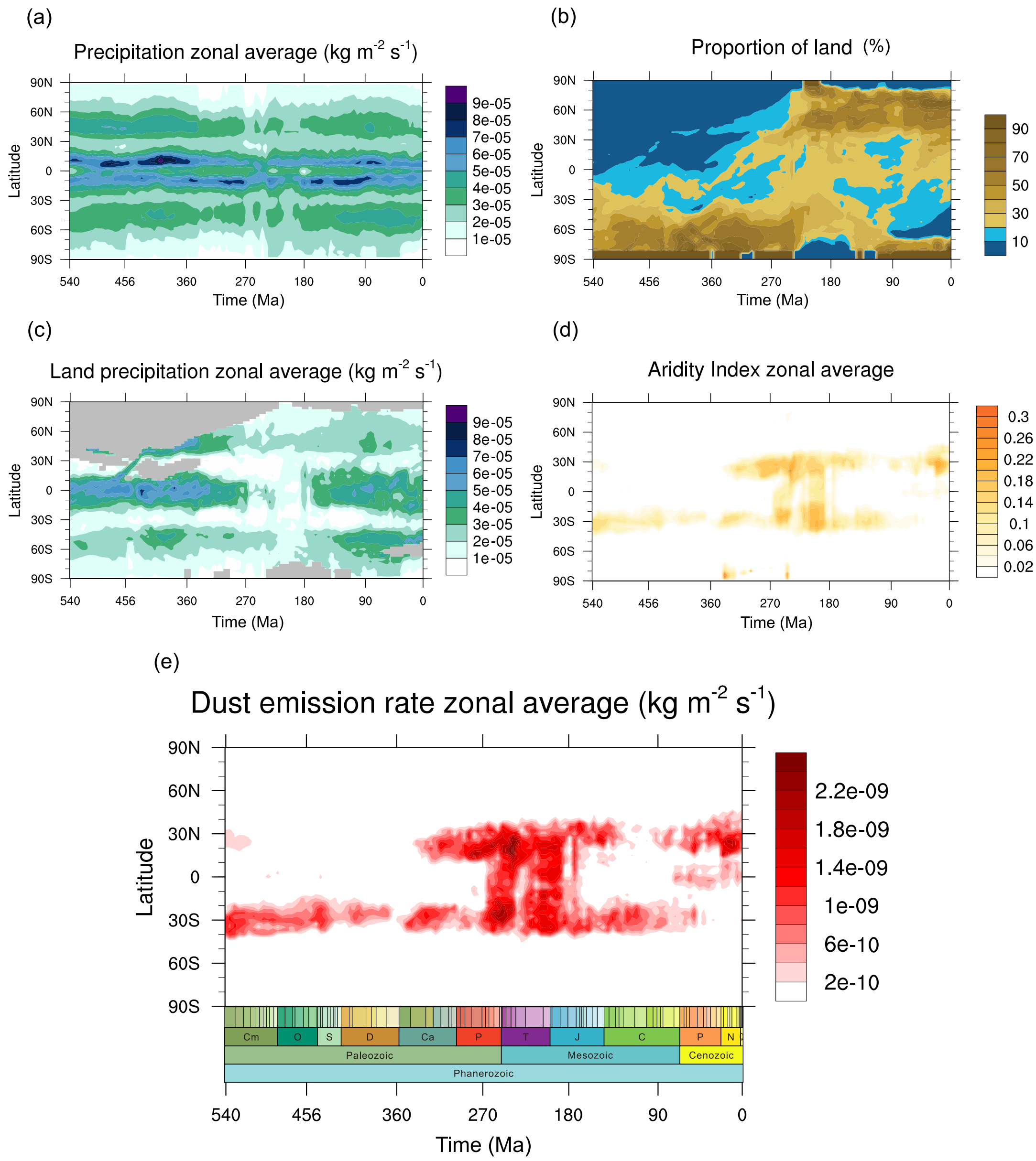

Figure 7. The zonal means of **(a)** the simulated precipitation, **(b)** the proportion of land , **(c)** the simulated precipitation over land, **(d)** the aridity index, **(e)** the simulated dust emissions over the Phanerozoic.

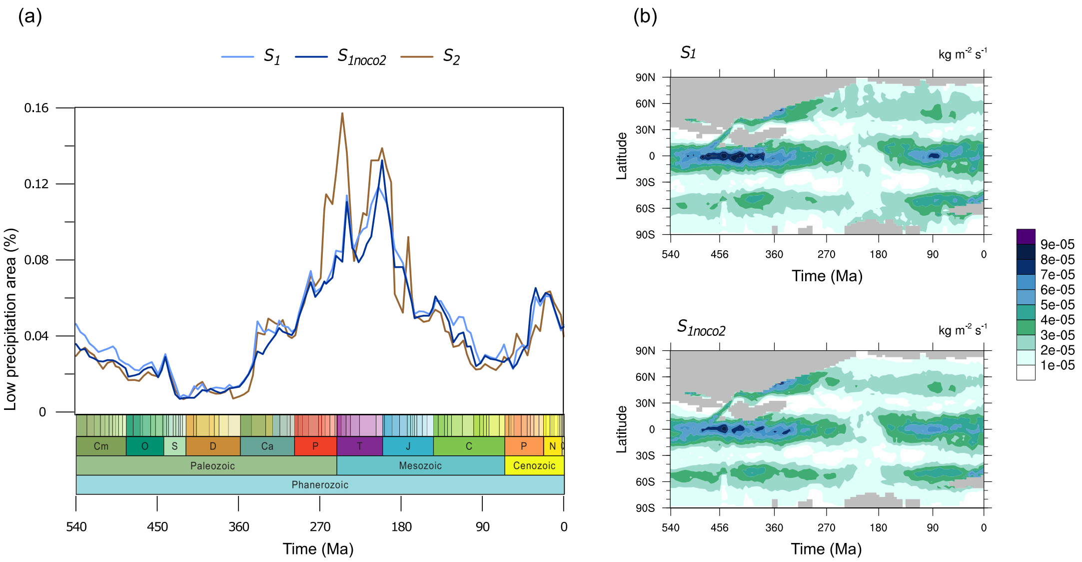

Figure 8. **(a)** Comparison of low precipitation area fraction time series from three different experimental series: S_1, S_1noco2 and S_2. A daily mean precipitation of less than 0.8 mm is considered low precipitation. **(b)** Comparison of zonal mean land precipitation over the Phanerozoic between experimental series S_1 and S_1noco2.

5 Discussion

5.1 Credibility of the simulated Phanerozoic dust

We herein compare evidence from both sediments and modelling to evaluate the simulated Phanerozoic dust emissions.

The evaporite sediment indicators compilation from ~~(Boucot et al., 2013), although not direct evidence of dust emissions,~~ Boucot et al. (2013) is used here to assess our ~~simulations because evaporites are indicators of arid regions due to its formation mechanism, and also the compilation gives continuous records covering the whole Phanerozoic .~~ simulation. This model-data comparison approach is indirect because evaporite is not a proxy for dust emission; however, it is chosen due to the absence of an appropriate proxy for dust emission, especially in deep-time paleo contexts. As a compromise, we compare the evaporite sediment records to the HadCM3L simulated evaporite, effectively evaluating the performance of the GCM in simulating the paleo hydrological cycles. The GCM predicts evaporation using the following criteria: mean annual precipitation less than 1400 mm, no more than 3 months with precipitation greater than 40 mm, and 6 months or more with mean temperature exceeding 20 °C (Craggs et al., 2012, scheme A). Similar evaporite prediction schemes are also used in Price et al. (1995); Bao et al. (2023) although they uses different criteria. This scheme roughly represents a rather arid environment in terms of its constraints on precipitation. Although the scheme is also temperature dependent, as has been argued in section 4.3 that atmospheric CO_2 induced hydroclimate change is neglectable, also considering that CO_2 is considered to be primarily driving the temperature change over the Phanerozoic (e.g. Mills et al., 2019; Royer et al., 2004), we ignore the effect from the temperature on evaporites predictions in the context of our focus on the hydrological cycles over the Phanerozoic timescale. This model-data comparison also serves as a side evaluation of the DUSTY1.0 model because the results from this study indicate that the dust emission is primarily dominated by the aridity (i.e. hydrological cycles) over the Phanerozoic (section 4.3).

How well the model matches with data is evaluated by how well the evaporite data in the compilation agree with estimates of potential evaporite distribution derived from the HadCM3L simulations. ~~There is uncertainty underlying this model-data comparison coming from the algorithm used for predicting evaporites from temperature and precipitation that cannot be quantified within this study.~~ Evaporite data points from Boucot et al. (2013) are rotated back to their paleo coordinates. We do not include data points that are outside the land mask in our paleogeograohy configuration, because the formation mechanism of those evaporites found on the coastline and continental shelf are mainly related to the marine incursion and thus do not represent arid paleoenvironment.

~~Notably, the modelled simulated widespread tropical drought – leading to widely distributed potential evaporites – during the late Permian to the early Jurassic (Figure 9ab) coordinates well with the geological sedimentary evidence. Quantitatively, the modelperformance~~ The performance of the model, indicated by the overlay ratio of evaporite data points on the model-predicted evaporite areas, varies over time~~, with an averageof~~ . On average, 35.3% of the evaporite data points ~~predicted correctly~~ are correctly predicted by the HadCM3L model over the Phanerozoic. To put this agreement in content, we also derive a "zero skill model", in which the fixed evaporite simulations for 0 Ma are applied for all ~~the paleo timeslices~~paleo timeslices, constraining the lowest performance limit from a random model prediction. The zero-skill model ~~gives an average~~ achieves an average agreement of 4.6%~~agreement, which is notably lower than what~~ , significantly lower than the HadCM3L ~~got, suggesting the fair good performance~~ model's performance, indicating the adequate accuracy of the model used ~~here~~ in this study (Figure 9e). Notably, the simulated widespread tropical drought during the late Permian to early Jurassic, which leads to widely distributed potential evaporites, corresponds fairly well with the geological sedimentary evidence (Figure 9ab), with an averaged overlay ratio of 67.7%.

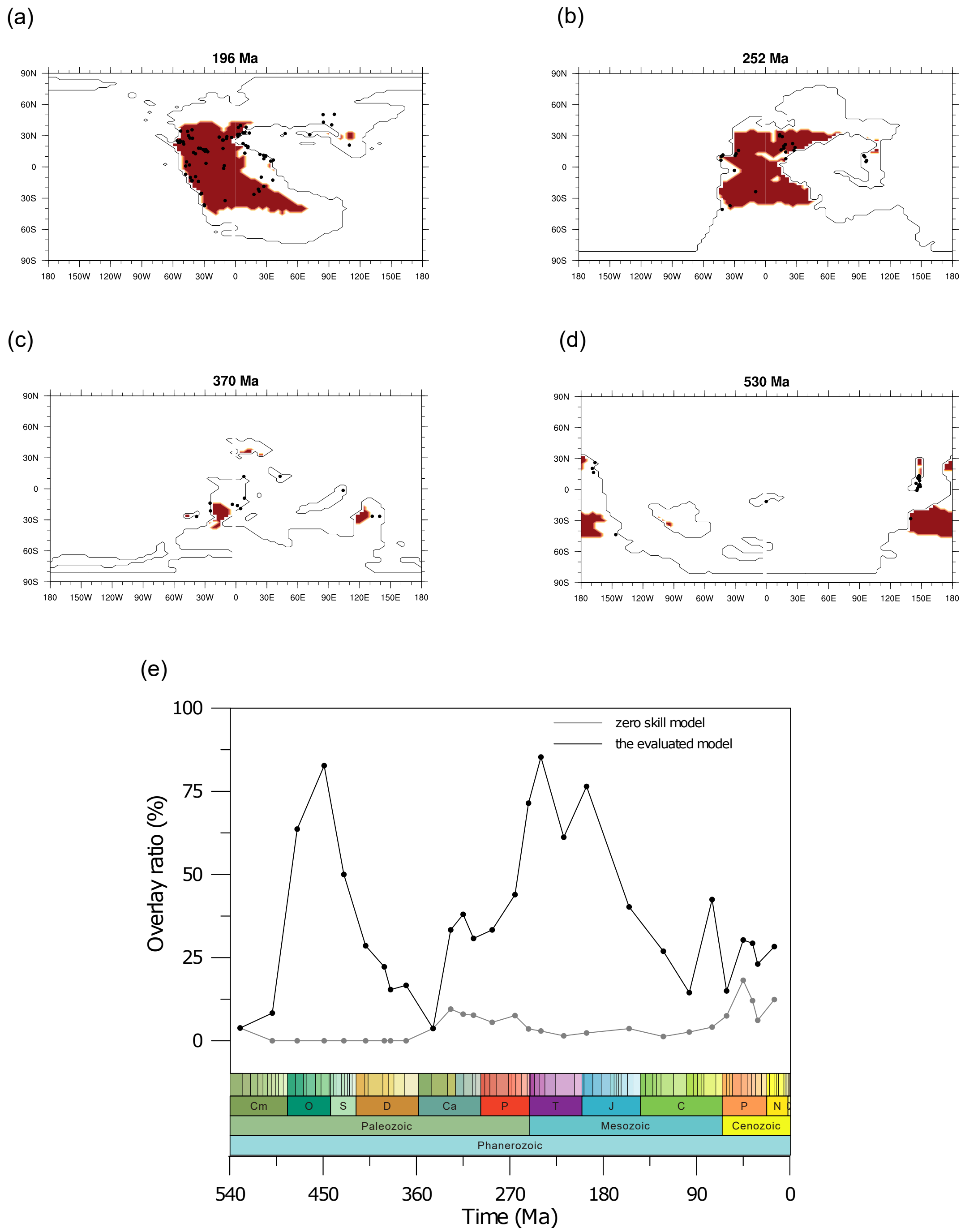

Figure 9. Comparisons of evaporite sedimentary records (dark dots, data from (Boucot et al., 2013)) to the simulated evaporite (area in red) of a few example time slices: **(a)** the early Jurassic (196 Ma), **(b)** the early Triassic (252 Ma), **(c)** the late Devonian (370 Ma), **(d)** the early Cambrian (530 Ma), and **(e)** a time series representing the performance of the model derived by assessing the overlap between model and data over time.

Here, we further focus on the Mesozoic to Cenozoic Asian ~~dessert~~ desert dust and the Mesozoic Pangean ~~dessert~~ desert dust to evaluate the accuracy of our simulations.

Our results show that the Asian ~~dessert~~ desert dust generated since the middle Jurassic (168 Ma), reached a maximum at the Late Jurassic–Early Cretaceous (145 Ma). During the early Cretaceous (131 - 97 Ma), the Asian continent passed through a period without obvious desert dust. The dust provenance then became very broad in subtropical Asia from the late Eocene (36 Ma) to the present. As documented in previous studies, the extreme Asian aridity evidenced from formations in the Junggar Basin of the Late Jurassic–Early Cretaceous (Jolivet et al., 2017) is well simulated from our results. Results from previous modelling studies show that central and western Asia was generally dry at the end of the Late Cretaceous, but was not identified as unvegetated dust provenance (Zhang et al., 2019). our results constrain the arid dust emission region to the central and west subtropical belt, which is also accordant to the proxy evidence of eolian dunes recorded in the earlier late Cretaceous (Farnsworth et al., 2019; Hasegawa et al., 2012). The permanent aridification recorded in the present-day Xining Basin originated from the late Eocene to Oligocene (40 Ma) (Licht et al., 2016; Bosboom et al., 2014), our simulations show the dust provenance appears since 36 Ma, which is in good agreement.

The dust emissions during the late Permian to the ~~lower Jurassic~~early Jurassic, as identified in this study, are remarkably high over the whole Phanerozoic. Our results suggest that the extensive dust emissions across the tropical and subtropical supercontinent ~~lasted~~ specifically occurred from 265 Ma to 190 Ma. Flora biome evidence and a general lack of plant fossil record (Nowak et al., 2020) supports the massive desert environment which was distributed almost identically to our simulated dust provenance during the late Permian (256 Ma). Sediment records (Boucot et al., 2013) indicate similar massive aridity patterns as our simulations – the sediments reflecting wet and semi-arid environments in the central tropical land were not documented ~~and~~ while the sediments reflecting arid environments were abundantly found along the edges of tropical and subtropical land since the Middle-Late Permian (265 Ma) to the middle Triassic (240 Ma) (Figure 9), suggesting a massive extreme arid extended from subtropic to tropic during the corresponding times.

5.2 Implication and Limitation

Our study for the first time presents the dust emission variations over the past 540 Million years with the dust emission fields for each of the 109 corresponding time slices, which can serve as an archive both in the field of dust simulations and ~~the~~ paleoclimate. Similar simulations focusing on deep-time dust variations have been performed by Lin et al. (2024) with a different GCM and vegetation scheme. Our results in general support their conclusion that subtropical land is the major controlling factor in the dust variations since the late Permian, and extend this mechanism to the whole Phanerozoic with higher temporal resolution experiments. Further model-data comparison and model-model comparison can be carried out on this basis in the future to improve the understanding of deep-time dust variations and their mechanisms.

~~For the time periods where our results show high dust emissions, the radiation effect of dust is presumably very different from the pre-industrial time or the Last Glacial Maximum. The latter two are relatively well constrained, whereas the effects in high-emission paleo times are worth further diagnosis.~~

Some of the bias from our results may arise from details about the dust emission process that have to be omitted in this study. As mentioned in section 2.1, the particle size and topography parameters are significant to the physical dust emission process but are not included here due to a lack of information. ~~Another aspect of bias is from the vegetation scheme used in our simulations~~

Uncertainties in our simulated results could have been caused by the vegetation simulations in different ways. We here in this study ~~assume~~ assumed plant functional types are consistent and the same as modern over the whole Phanerozoic ~~, which~~ with applying the TRIFFID interactive vegetation model to all paleo time slices. This will theoretically result in inappropriate vegetation outputs~~in the deep-time paleo.~~ , especially in the older time results. To constrain the uncertainty during the time before land plant colonization, we carry out sensitive tests by running the DUSTY1.0 model with the assumption that all land areas are non-vegetated areas, except for those prescribed as ice sheets, prior to the end of Devonian (360 Ma) (Figure 10). Sensitivity tests reveal that results shown in section 4.1 underestimate the dust emissions over the early-Paleozoic times, with a factor of doubling underestimate at the Ordovician-Silurian transition emission peak and about two times underestimate at the early Devonian emission peak, whereas for most of the other early Paleozoic times, the level of underestimation is mostly within the range of 5% to 30%. The degree of underestimation is not as significant as the decomposed contributions from the non-vegetated area b derived in section 4.2. This is because of the coupled variations between vegetation and soil moisture. Even with the assumption of no land vegetation, the simulated areas of desert dust are similarly constrained by the soil moisture. However, there is a bias in these estimations of uncertainty because the dynamic interactions between vegetation and climate are neglected, which possibly explains the discrepancy compared to the up to fourfold underestimation in the Precambrian (Liu et al., 2020). A more accurate evaluation of underestimation could be done by running the GCM simulations without the TRIFFID scheme. Due to the matter of computational cost, this is not performed within this study. Moreover, the lack of vegetation would likely also result in a very different land surface during these times, which may also have a big impact on emission properties. Our simulations after the Devonian (360 Ma) are ~~supposed to be~~ more robust than those prior to that when terrestrial flora ~~was perhaps~~ is more similar to today. While this constant vegetation scheme is the common approach of most current paleoclimate modelling studies, the new trait-based whole-plant functional-strategy approach (Matthaeus et al., 2023) shows potential to be an alternative solution. ~~Regarding the~~ The scope of this study ~~is~~ has focused on only looking at the non-vegetated area rather than a specific vegetation type, despite the unavoidable uncertainties coming with the vegetation scheme, We argue that the modelled dust and aridity are relatively robust, as any vegetation may have flourished where there was precipitation.

Another aspect of uncertainties caused by the vegetation scheme is related to the atmospheric CO_2. The vegetation model TRIFFID predicts plant functional types by taking atmospheric CO_2 in addition to temperature and precipitation from the GCM, and a higher CO_2 will fertilize the vegetation. As such, we emphasise the uncertainties of our simulated dust emissions, presumably underestimations, for the periods before 420 Ma, when the CO2 forcings are derived from an "extension" of the Foster et al. (2017) data and appear very high (Valdes et al., 2020). The explicit effects of CO_2 on vegetation could be explored by running the vegetation model offline with consistent temperature and precipitation but different CO_2, which could be tested in future research.

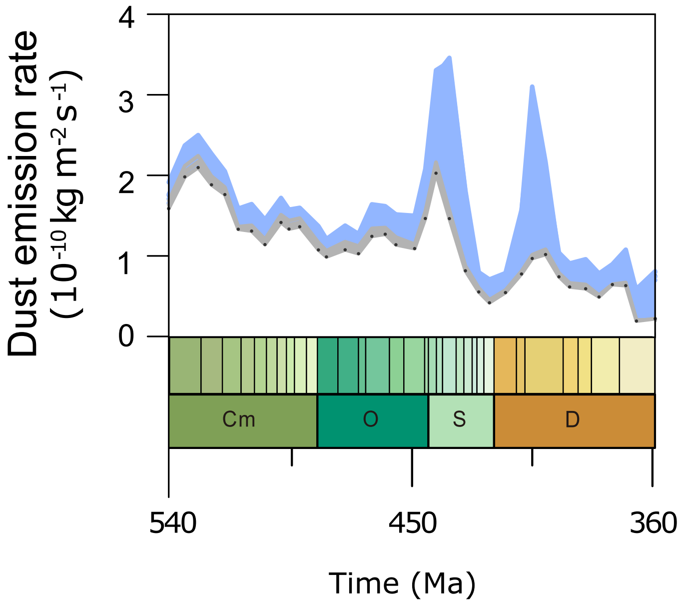

Figure 10. The uncertainty of dust emission rates tested by assuming there is no land plant prior to the end of Devonian, as shown in blue shading. The grey shading is the simulated dust emissions identical to those illustrated in Figure 3.

In this study, the dust emission model does not give a complete dust cycle, nor is it fully coupled to the GCM, so the dust feedback is not represented in the simulations. The effect of dust on the corresponding paleo climate could have been significant, especially for periods with enormous emissions. ~~There have been many models do include the~~ For the time periods where our results show high dust emissions, the radiation effect of dust may be very different from the pre-industrial time or the Last Glacial Maximum. The latter two are relatively well constrained, whereas the effects in high-emission deeper times require further diagnosis. There are many models which include a dust scheme (e.g. the CMIP6 models evaluated in ~~(Zhao et al., 2022)~~ ~~, and~~ Zhao et al. (2022), but would take huge computational resources to run simulations of similar temporal resolution due to their complexity, while offline dust models are more suitable for carrying out multi-scale simulations with the defect of losing dynamic feedback between the dust cycle and the climate system. In addition, these models often require much greater detail of dust input parameters that is possible for the deep past.

Another aspect of limitation is the model designed for this study is not supposed to test the hypothesis related to the sediment supply process, e.g. the hydrological basins and glaciogenic dust source, as described in section 2.1. These explorations could be pursued in future research with higher computational resources, using more complex models including those parameterizations.

6 Conclusions

~~In this study, we take advantage of a series of paleoclimate simulations carried out with the Earth System Model which cover 109 time slices over the whole Phanerozoic, and extend the experiments to dust emissions of the same resolutions with a newly developed~~ In this study, we simulate dust emissions over the Phanerozoic with an offline dust emission model ~~–~~

DUSTY1.0 and the General Circulation Model HadCM3L. The dust emission model is first tuned to the modern and then applied to the paleo configurations. For the first time, ~~Our~~ our study yields a ~~time-series~~ timeseries of global dust emission rates of the whole Phanerozoic, along with corresponding dust emission fields at the stage level resolution. ~~Our results are evaluated by comparing them with sedimentary and plant fossil indicators~~The early Paleozoic may have underestimated simulated dust emissions before land plant colonization. Model-data comparisons reveal that our simulations are ~~in fair~~ reasonable in accordance with geological records.

The driving forces of dust emissions over time are analysed at different levels of mechanisms. From the perspective of dust emission-related surface processes, our results suggest the non-vegetated area is the predominant contributing factor to the multi-million-year-scale dust emissions variations, both in magnitude and in patterns of changes versus time. From the perspective of the geological timescale, our results suggest ~~the CO~~that paleogeography dominates the variations in continent aridity and, therefore, dust emissions, while the effect from CO_2 ~~effect on dust emissions is negligible compared to the effect from paleogeography~~ is negligible.

~~The key non-vegetated area driving factor draws the focus to the paleohydroclimate. Our results show the meridional precipitation patterns are rather stable throughout the Phanerozoic – more precipitation over the tropics and rare precipitation over the subtropics. Thus the mechanism of aridity area anddust emissions are explained by the continental land movement, the distance of land area to the closest sea in tropic and subtropic zones.~~

Code and data availability. The DUSTY1.0 model code is available and the simulated dust emissions fields are available from https://github.com/yixuan-coding/DUSTY1.0

Appendix A: Appendix

Here we provide the detailed methods of factorisation used in section 4.2.

For the linear factorisation on l and b. The dust emissions contributed by l (ΔD^l) is calculated by:

$$\Delta D^l = D^l \tag{A1}$$

representing the dust emissions difference between the configuration in which there is no dust emission over the whole globe, and the configuration in which all the land area produces dust. The corresponding states of other variables in the configuration in which all land is vegetation-free are: $b = 1$, which means all the land surface is covered by 100% bare soil; $m = 0$, which means the surface soil is at its driest over all land; $s = 0$, which means there is no snow cover anywhere; $U = 1.91$ (in the choice of tuned parameter set version 1), indicating the surface wind speed that blows up the dust. Similarly, the dust emissions contributed by b (ΔD^b) is calculated by:

$$\Delta D^b = D^{lb} - D^l, \tag{A2}$$

which represents the difference in dust emission rate between the configuration in which all land is vegetation-free and the configuration in which dust sources are restricted to non-vegetated land areas. The corresponding states of other variables in this configuration are identical to those in the all land is vegetation-free configuration except that b is assigned specific values.

For the non-linear factorisation on d_m, d_s and d_U, the algorithm is as follows according to ~~(Lunt et al., 2021)~~ Lunt et al. (2021) to calculate the difference between D and ΔD^{lb} :

The resulting equations for the factorisations are :

$$\begin{aligned}
\Delta D^m &= \frac{1}{6}\left[2(D^{lbm} - D^{lb}) + (D^{lbmU} - D^{lbU}) + (D^{lbms} - D^{lbs}) + 2(D^{lbmsU} - D^{lbsU})\right] \\
\Delta D^s &= \frac{1}{6}\left[2(D^{lbs} - D^{lb}) + (D^{lbms} - D^{lbm}) + (D^{lbsU} - D^{lbU}) + 2(D^{lbmsU} - D^{lbU})\right] \\
\Delta D^U &= \frac{1}{6}\left[2(D^{lbU} - D^{lb}) + (D^{lbmU} - D^{lbm}) + (D^{lbsU} - D^{lbs}) + 2(D^{lbmsU} - D^{lbms})\right]
\end{aligned} \tag{A3}$$

where the ΔD^m, ΔD^s and ΔD^U represent the difference in dust emission caused by the m, s and U from the "~~all-bare-land-dessert~~all-ba configuration respectively.

The total dust emission rate is hence isolated as:

$$D = \Delta D^l + \Delta D^b + \Delta D^m + \Delta D^s + \Delta D^U \tag{A4}$$

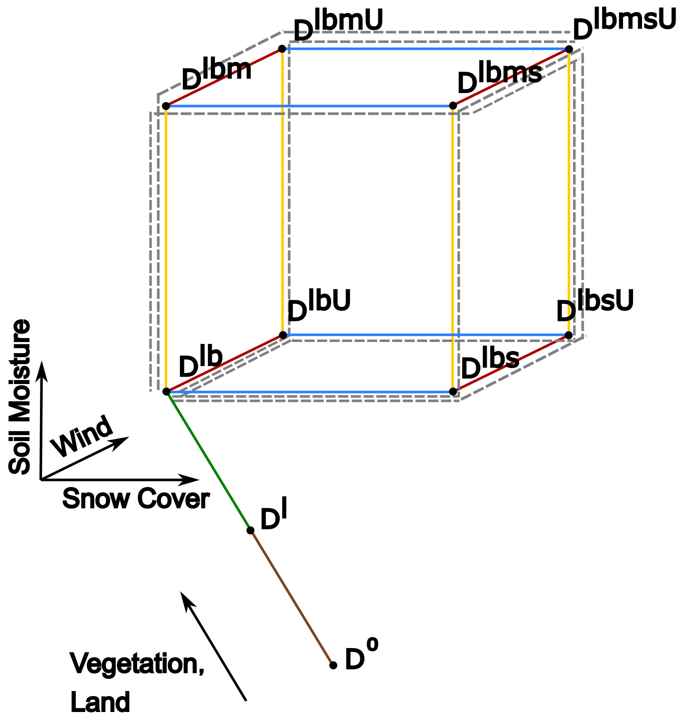

Figure A1. The factorisation method concept

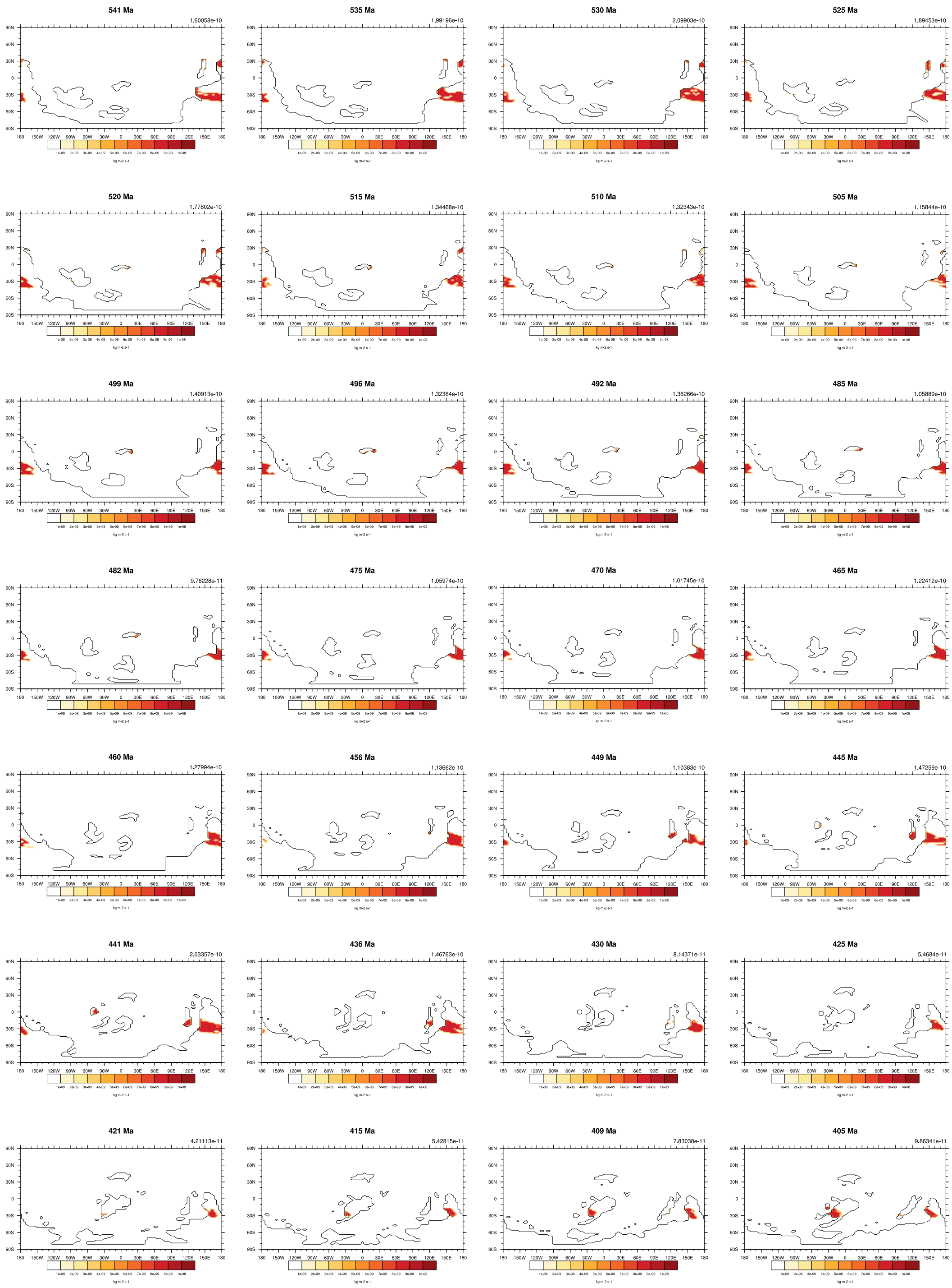

Figure A2. The simulated dust emissions of all 109 time slices over the Phanerozoic (Part 1). Values at the top-right are the global mean dust emission rates. Unites are $kg\ m^{-2}s^{-1}$.

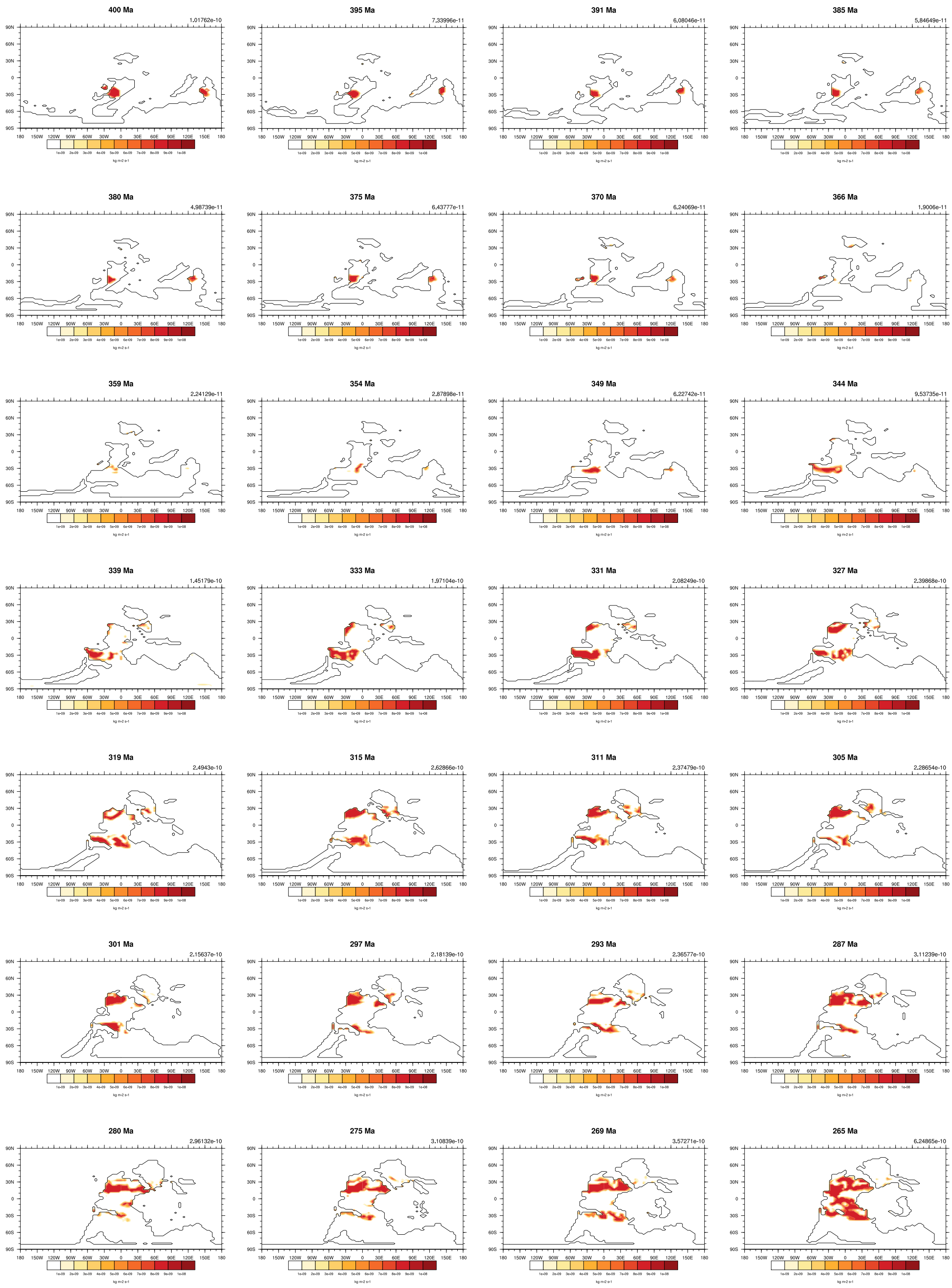

Figure A3. The simulated dust emissions of all 109 time slices over the Phanerozoic (Part 2). Values at the top-right are the global mean dust emission rates. Unites are $kg\ m^{-2}s^{-1}$.

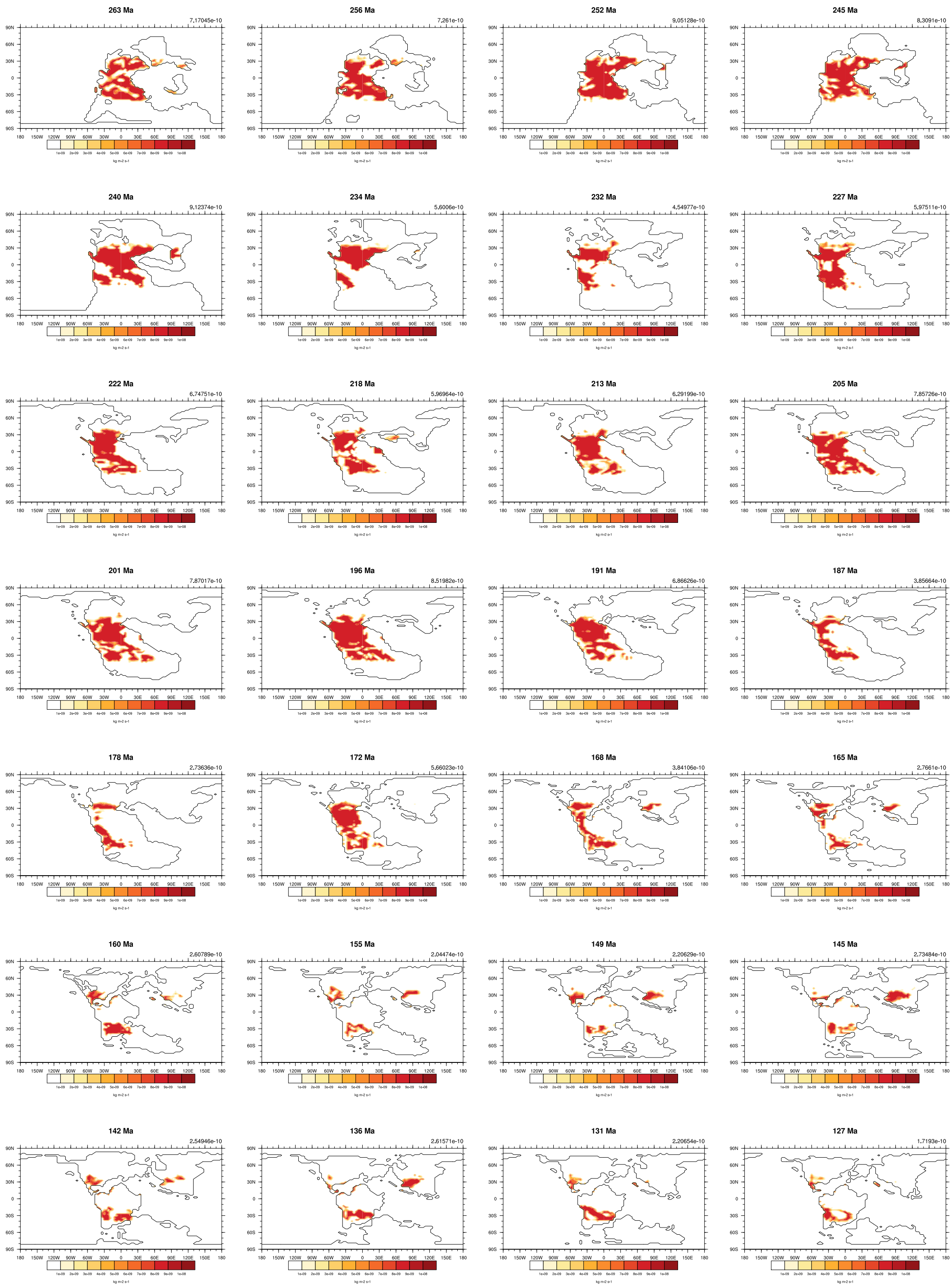

Figure A4. The simulated dust emissions of all 109 time slices over the Phanerozoic (Part 3). Values at the top-right are the global mean dust emission rates. Unites are $kg\, m^{-2} s^{-1}$.

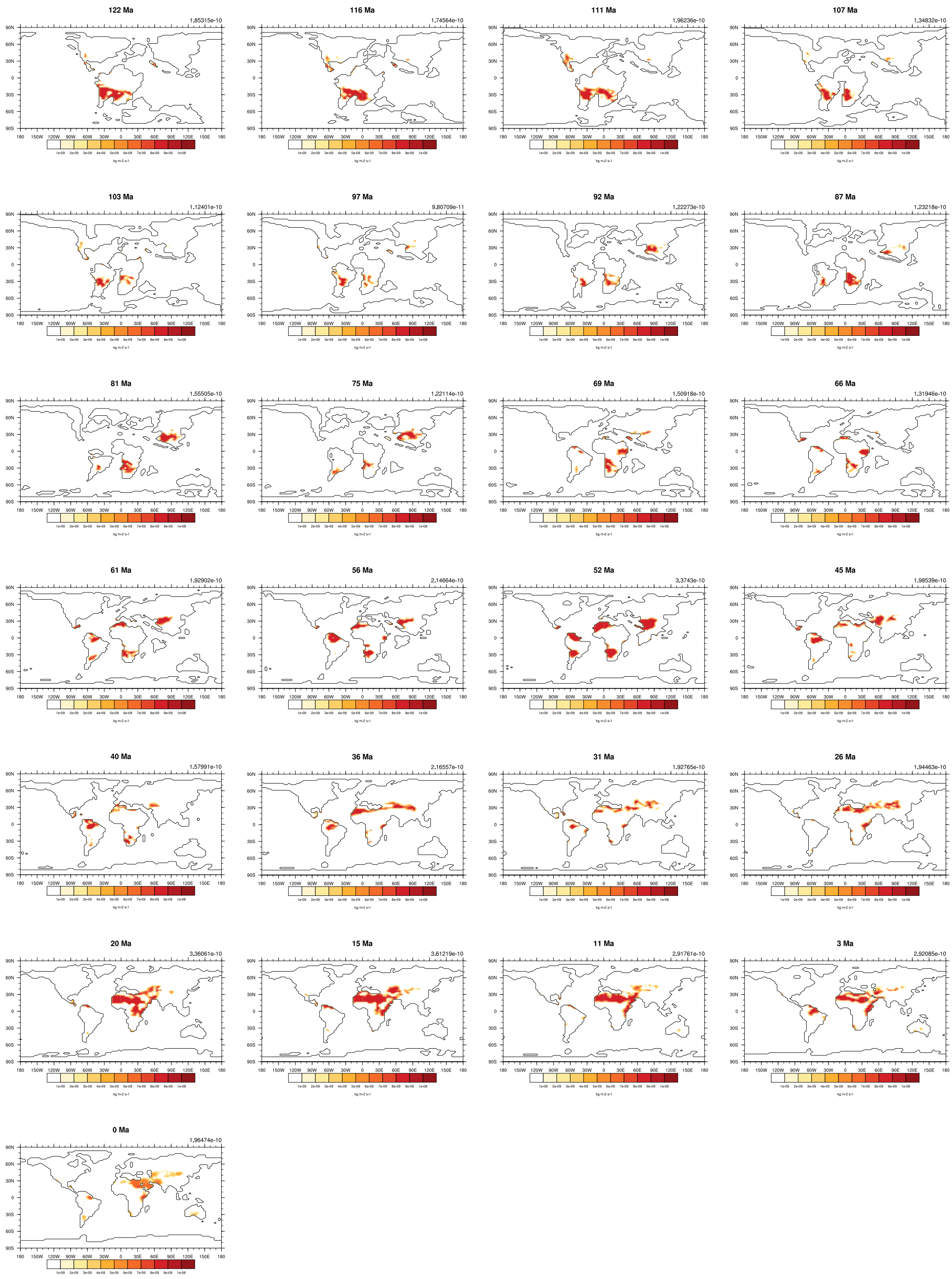

Figure A5. The simulated dust emissions of all 109 time slices over the Phanerozoic (Part 4). Values at the top-right are the global mean dust emission rates. Unites are $kg\, m^{-2} s^{-1}$.

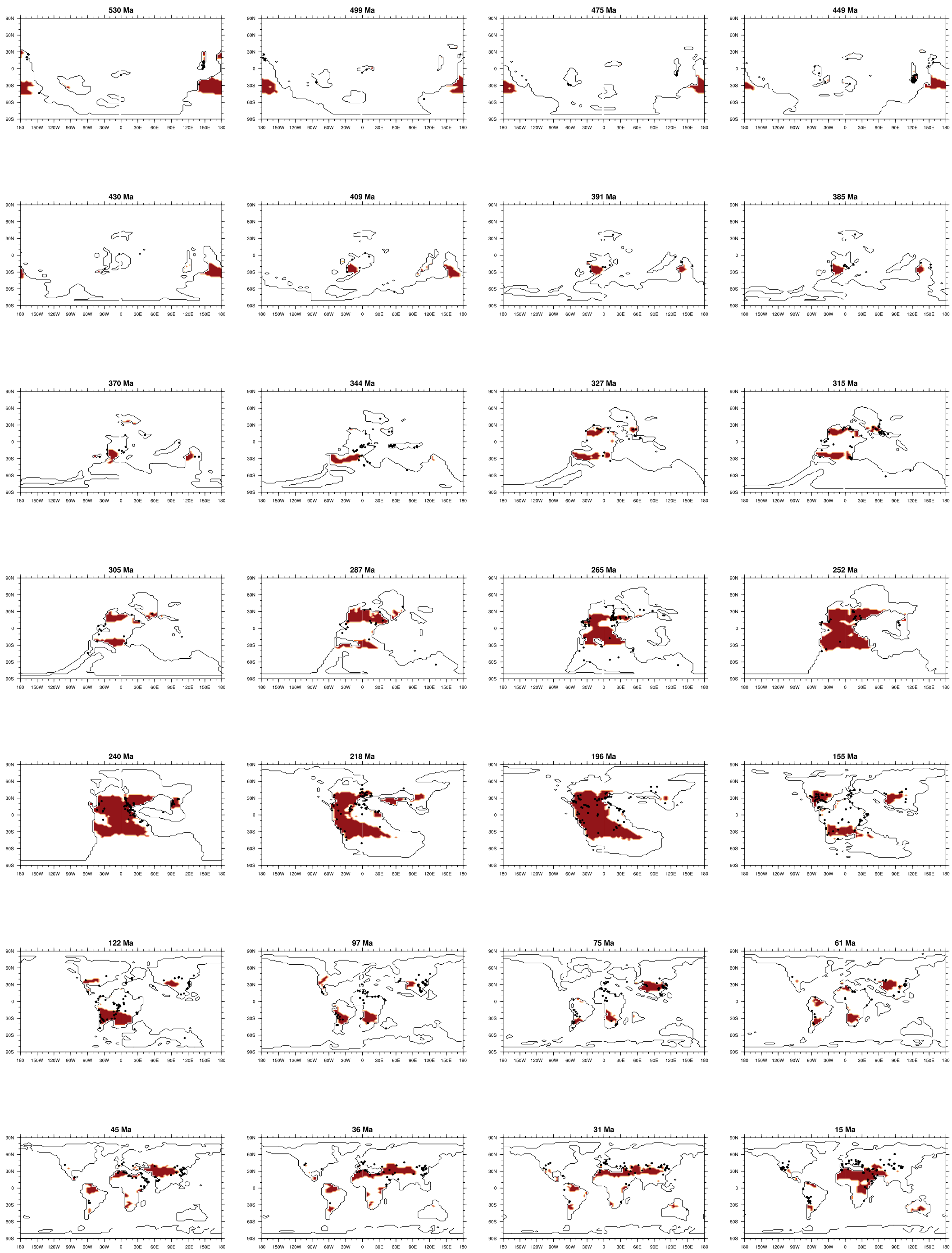

Figure A6. Comparisons of evaporite sedimentary records (dark dots, data from (Boucot et al., 2013)) to the simulated evaporite (area in red) of multiple time slices

Author contributions. The study was developed by all authors. PJV and DJL performed the original HadCM3L model simulations. DJL and YX designed the study, developed the DUSTY1.0 model and carried out the analysis.YX wrote the original manuscript, DJL and PJV provided edits .

Competing interests. The authors declare that they have no conflict of interest.

Acknowledgements. DJL and PJV acknowledge NERC grant NE/X000222/1 (PaleoGradPhan: Paleoclimate meridional and zonal Gradients in the Phanerozoic). YX acknowledges funding from the China Scholarship Council (Grant No. 202006380069).

References

Anderson, C. H., Murray, R. W., Dunlea, A. G., Giosan, L., Kinsley, C. W., McGee, D., and Tada, R.: Aeolian delivery to Ulleung Basin, Korea (Japan Sea), during development of the East Asian Monsoon through the last 12 Ma, Geological Magazine, 157, 806–817, https://doi.org/10.1017/S001675681900013X, 2020.

Arakawa, A. and Lamb, V. R.: Computational Design of the Basic Dynamical Processes of the UCLA General Circulation Model, in: General Circulation Models of the Atmosphere, edited by CHANG, J., vol. 17 of *Methods in Computational Physics: Advances in Research and Applications*, pp. 173–265, Elsevier, https://doi.org/https://doi.org/10.1016/B978-0-12-460817-7.50009-4, 1977.

Bao, X., Hu, Y., Scotese, C. R., Li, X., Guo, J., Lan, J., Lin, Q., Yuan, S., Wei, M., Li, Z., Man, K., Yin, Z., Han, J., Zhang, J., Wei, Q., Liu, Y., Yang, J., and Nie, J.: Quantifying climate conditions for the formation of coals and evaporites, National Science Review, 10, https://doi.org/10.1093/nsr/nwad051, 2023.

Bosboom, R. E., Abels, H. A., Hoorn, C., van den Berg, B. C., Guo, Z. J., and Dupont-Nivet, G.: Aridification in continental Asia after the Middle Eocene Climatic Optimum (MECO), Earth and Planetary Science Letters, 389, 34–42, https://doi.org/10.1016/j.epsl.2013.12.014, 2014.

Boucot, A. J., Xu, C., Scotese, C. R., and Morley, R. J.: Phanerozoic Paleoclimate: An Atlas of Lithologic Indicators of Climate, SEPM Concepts in Sedimentology and Paleontology, 11, SEPM (Society for Sedimentary Geology) Tulsa, OK, ISBN 9781565762817, https://pubs.geoscienceworld.org/books/book/1966/, 2013.

Bullard, J. E., Baddock, M., Bradwell, T., Crusius, J., Darlington, E., Gaiero, D., Gassó, S., Gisladottir, G., Hodgkins, R., McCulloch, R., McKenna-Neuman, C., Mockford, T., Stewart, H., and Thorsteinsson, T.: High-latitude dust in the Earth system, https://doi.org/10.1002/2016RG000518, 2016.

Bushell, A.: Unified Model User Guide, chap. Clouds, p. 27, in: Matthews, https://gmd.copernicus.org/preprints/gmd-2017-16/gmd-2017-16.pdf, 1998.

Cakmur, R. V., Miller, R. L., Perlwitz, J., Geogdzhayev, I. V., Ginoux, P., Koch, D., Kohfeld, K. E., Tegen, I., and Zender, C. S.: Constraining the magnitude of the global dust cycle by minimizing the difference between a model and observations, 111, 1–24, https://doi.org/10.1029/2005JD005791, 2006.

Cecil, C. B.: The Concept of Autocyclic and Allocyclic Controls on Sedimentation and Stratigraphy, Emphasizing the Climatic Variable, https://doi.org/10.2110/pec.03.77.0013, 2003.

Charney, J., Quirk, W. J., Chow, S. H., and Kornfield, J.: Comparative Study of the Effects of Albedo Change on Drought in Semi-Arid Regions., https://doi.org/10.1175/1520-0469(1977)034<1366:ACSOTE>2.0.CO;2, 1977.

Chen, S., Huang, J., Qian, Y., Zhao, C., Kang, L., Yang, B., Wang, Y., Liu, Y., Yuan, T., Wang, T., Ma, X., and Zhang, G.: An overview of mineral dust modeling over East Asia, Journal of Meteorological Research, 31, 633–653, https://doi.org/10.1007/s13351-017-6142-2, 2017.

Cox, M. D., Oceanic, G. F. D. L. N., and Administration), A.: A Primitive Equation, 3-dimensional Model of the Ocean, GFDL Ocean Group technical report, Geophysical Fluid Dynamica Laboratory/NOAA, Princeton University, https://books.google.co.uk/books?id=ayfaxwEACAAJ, 1984.

Cox, P., Betts, R., Bunton, C., Essery, R., Rowntree, P., and Smith, J.: The impact of new land surface physics on the GCM simulation of climate and climate sensitivity, Climate Dynamics, 15, 183–203, https://doi.org/10.1007/s003820050276, 1999.

Craggs, H. J., Valdes, P. J., and Widdowson, M.: Climate model predictions for the latest Cretaceous: An evaluation using climatically sensitive sediments as proxy indicators, Palaeogeography, Palaeoclimatology, Palaeoecology, 315-316, 12–23, https://doi.org/10.1016/j.palaeo.2011.11.004, 2012.

DeCelles, P. G., Kapp, P., Ding, L., and Gehrels, G. E.: Late Cretaceous to middle Tertiary basin evolution in the central Tibetan Plateau: Changing environments in response to tectonic partitioning, aridification, and regional elevation gain, GSA Bulletin, 119, 654–680, https://doi.org/10.1130/B26074.1, 2007.

Diaz, H. F. and Bradley, R. S.: The Hadley circulation: Present, past, and future: An introduction, in: The Hadley circulation: present, past and future, pp. 1–5, Springer, 2004.

Edwards, J. M. and Slingo, A.: Studies with a flexible new radiation code. I: Choosing a configuration for a large-scale model, Quarterly Journal of the Royal Meteorological Society, 122, 689–719, https://doi.org/https://doi.org/10.1002/qj.49712253107, 1996.

Farnsworth, A., Lunt, D. J., Robinson, S. A., Valdes, P. J., Roberts, W. H., Clift, P. D., Markwick, P., Su, T., Wrobel, N., Bragg, F., Kelland, S. J., and Pancost, R. D.: Past East Asian monsoon evolution controlled by paleogeography, not CO2, Tech. Rep. 10, ISSN 23752548, https://doi.org/10.1126/sciadv.aax1697, 2019.

Fitzsimmons, K. E., Cohen, T. J., Hesse, P. P., Jansen, J., Nanson, G. C., May, J. H., Barrows, T. T., Haberlah, D., Hilgers, A., Kelly, T., Larsen, J., Lomax, J., and Treble, P.: Late Quaternary palaeoenvironmental change in the Australian drylands, Quaternary Science Reviews, 74, 78–96, https://doi.org/10.1016/J.QUASCIREV.2012.09.007, 2013.

Foster, G. L., Royer, D. L., and Lunt, D. J.: Future climate forcing potentially without precedent in the last 420 million years, Nature Communications, 8, 1–8, https://doi.org/10.1038/ncomms14845, 2017.

Gabbott, S. E., Zalasiewicz, J., Aldridge, R. J., and Theron, J. N.: Eolian input into the Late Ordovician postglacial Soom Shale, South Africa, Geology, 38, 1103–1106, https://doi.org/10.1130/G31426.1, 2010.

Gillette, D. A. and Passi, R.: Modeling dust emission caused by wind erosion, Journal of Geophysical Research, 93, https://doi.org/10.1029/jd093id11p14233, 1988.

Ginoux, P., Chin, M., Tegen, I., Goddard, T., and In, G.: Sources and distributions of dust aerosols simulated with the GOCART model, ournal of Geophysical Research, 106, 20 255–20 273, 2001.

Gkikas, A., Proestakis, E., Amiridis, V., Kazadzis, S., Di Tomaso, E., Tsekeri, A., Marinou, E., Hatzianastassiou, N., and Pérez Garciá-Pando, C.: ModIs Dust AeroSol (MIDAS): A global fine-resolution dust optical depth data set, Atmospheric Measurement Techniques, 14, 309–334, https://doi.org/10.5194/amt-14-309-2021, 2021.

Gough, D. O.: Solar interior structure and luminosity variations, Solar Physics, 74, 21–34, https://doi.org/10.1007/BF00151270, 1981.

Gregory, D., Kershaw, R., and Inness, P. M.: Parametrization of momentum transport by convection. II: Tests in single-column and general circulation models, Quarterly Journal of the Royal Meteorological Society, 123, 1153–1183, https://doi.org/https://doi.org/10.1002/qj.49712354103, 1997.

Hasegawa, H., Tada, R., Jiang, X., Suganuma, Y., Imsamut, S., Charusiri, P., Ichinnorov, N., and Khand, Y.: Drastic shrinking of the Hadley circulation during the mid-Cretaceous Supergreenhouse, Climate of the Past, 8, 1323–1337, https://doi.org/10.5194/cp-8-1323-2012, 2012.

Jickells, T. D., An, Z. S., Andersen, K. K., Baker, A. R., Bergametti, C., Brooks, N., Cao, J. J., Boyd, P. W., Duce, R. A., Hunter, K. A., Kawahata, H., Kubilay, N., LaRoche, J., Liss, P. S., Mahowald, N., Prospero, J. M., Ridgwell, A. J., Tegen, I., and Torres, R.: Global iron connections between desert dust, ocean biogeochemistry, and climate, Tech. Rep. 5718, ISSN 00368075, https://doi.org/10.1126/science.1105959, 2005.

Jolivet, M., Bourquin, S., Heilbronn, G., Robin, C., Barrier, L., Dabard, M. P., Jia, Y., De Pelsmaeker, E., and Fu, B.: The Upper Jurassic-Lower Cretaceous alluvial-fan deposits of the Kalaza Formation (Central Asia): Tectonic pulse or increased aridity?, Geological Society Special Publication, 427, 491–521, https://doi.org/10.1144/SP427.6, 2017.

Jones, L. A., Mannion, P. D., Farnsworth, A., Bragg, F., and Lunt, D. J.: Climatic and tectonic drivers shaped the tropical distribution of coral reefs, Nature Communications, 13, 1–10, https://doi.org/10.1038/s41467-022-30793-8, 2022.

Kerkweg, A., Sander, R., Tost, H., and Jöckel, P.: Technical note: Implementation of prescribed (OFFLEM), calculated (ONLEM), and pseudo-emissions (TNUDGE) of chemical species in the Modular Earth Submodel System (MESSy), Atmospheric Chemistry and Physics, 6, 3603–3609, https://doi.org/10.5194/acp-6-3603-2006, 2006.

Kiehl, J. T. and Shields, C. A.: Sensitivity of the palaeocene-eocene thermal maximum climate to cloud properties, Philosophical Transactions of the Royal Society A: Mathematical, Physical and Engineering Sciences, 371, https://doi.org/10.1098/rsta.2013.0093, 2013.

Kohfeld, K. E. and Harrison, S. P.: DIRTMAP: The geological record of dust, Earth-Science Reviews, 54, 81–114, https://doi.org/10.1016/S0012-8252(01)00042-3, 2001.

Kok, J. F., Parteli, E. J., Michaels, T. I., Karam, D. B., R Parteli, E. J., Michaels, T. I., Bou Karam, D., F, K. J., J R, P. E., I, M. T., and Karam, B. D.: The physics of wind-blown sand and dust, vol. 75, https://doi.org/10.1088/0034-4885/75/10/106901, 2012.

Kok, J. F., Mahowald, N. M., Fratini, G., Gillies, J. A., Ishizuka, M., Leys, J. F., Mikami, M., Park, M. S., Park, S. U., Van Pelt, R. S., and Zobeck, T. M.: An improved dust emission model - Part 1: Model description and comparison against measurements, Atmospheric Chemistry and Physics, 14, 13 023–13 041, https://doi.org/10.5194/acp-14-13023-2014, 2014.

Lamy, F., Gersonde, R., Winckler, G., Esper, O., Jaeschke, A., Kuhn, G., Ullermann, J., Martínez-Garcia, A., Lambert, F., and Kilian, R.: Increased dust deposition in the Pacific Southern Ocean during glacial periods, Science, 343, 403–407, 2014.

Li, Y., Shi, W., Aydin, A., Beroya-Eitner, M. A., and Gao, G.: Loess genesis and worldwide distribution, Earth-Science Reviews, 201, 102 947, https://doi.org/https://doi.org/10.1016/j.earscirev.2019.102947, 2020.

Licht, A., Dupont-Nivet, G., Pullen, A., Kapp, P., Abels, H. A., Lai, Z., Guo, Z., Abell, J., and Giesler, D.: Resilience of the Asian atmospheric circulation shown by Paleogene dust provenance, Nature Communications, 7, https://doi.org/10.1038/ncomms12390, 2016.

Lin, Q., Liu, Y., Guo, J., Li, X., Lan, J., Zuo, H., Zhang, M., Zhang, J., Zhao, Z., Yuan, S., Bao, X., and Hu, Y.: Simulated dust activity in typical time periods of the past 250 million years, Fundamental Research, https://doi.org/10.1016/j.fmre.2024.02.004, 2024.

Liu, P., Liu, Y., Peng, Y., Lamarque, J. F., Wang, M., and Hu, Y.: Large influence of dust on the Precambrian climate, Nature Communications, 11, 1–8, https://doi.org/10.1038/s41467-020-18258-2, 2020.

Lunt, D. J. and Valdes, P. J.: The modern dust cycle: Comparison of model results with observations and study of sensitivities, Journal of Geophysical Research Atmospheres, 107, 1–1, https://doi.org/10.1029/2002JD002316, 2002.

Lunt, D. J., Chandan, D., Haywood, A. M., Lunt, G. M., Rougier, J. C., Salzmann, U., Schmidt, G. A., and Valdes, P. J.: Multi-variate factorisation of numerical simulations, Geoscientific Model Development, 14, 4307–4317, https://doi.org/10.5194/gmd-14-4307-2021, 2021.

Mahowald, N. M., Muhs, D. R., Levis, S., Rasch, P. J., Yoshioka, M., Zender, C. S., and Luo, C.: Change in atmospheric mineral aerosols in response to climate: Last glacial period, preindustrial, modern, and doubled carbon dioxide climates, Journal of Geophysical Research: Atmospheres, 111, https://doi.org/https://doi.org/10.1029/2005JD006653, 2006.

Mahowald, N. M., Scanza, R., Brahney, J., Goodale, C. L., Hess, P. G., Moore, J. K., and Neff, J.: Aerosol Deposition Impacts on Land and Ocean Carbon Cycles, Current Climate Change Reports, 3, 16–31, https://doi.org/10.1007/s40641-017-0056-z, 2017.

Marx, S. K., Kamber, B. S., McGowan, H. A., Petherick, L. M., McTainsh, G. H., Stromsoe, N., Hooper, J. N., and May, J. H.: Palaeo-dust records: A window to understanding past environments, Global and Planetary Change, 165, 13–43, https://doi.org/10.1016/j.gloplacha.2018.03.001, 2018.

Marzocchi, A., Lunt, D. J., Flecker, R., Bradshaw, C. D., Farnsworth, A., and Hilgen, F. J.: Orbital control on late Miocene climate and the North African monsoon: insight from an ensemble of sub-precessional simulations, Climate of the Past, 11, 1271–1295, https://doi.org/10.5194/cp-11-1271-2015, 2015.

Matthaeus, W. J., Macarewich, S. I., Richey, J., Montañez, I. P., Mcelwain, J. C., White, J. D., Wilson, J. P., and Poulsen, C. J.: A Systems Approach to Understanding How Plants Transformed Earth's Environment in Deep Time, Annual Review of Earth and Planetary Sciences, 51, 551–580, https://doi.org/10.1146/annurev-earth-080222-082017, 2023.

McGlannan, A. J., Bonar, A., Pfeifer, L., Steinig, S., Valdes, P., Adams, S., Duarte, D., Milad, B., Cullen, A., and Soreghan, G. S.: An eolian dust origin for clastic fines of Devono-Mississippian mudrocks of the greater North American midcontinent, Journal of Sedimentary Research, 92, 1186–1206, https://doi.org/10.2110/jsr.2022.013, 2022.

Mckay, M., Beckman, R., and Conover, W.: A Comparison of Three Methods for Selecting Vales of Input Variables in the Analysis of Output From a Computer Code, Technometrics, 21, 239–245, https://doi.org/10.1080/00401706.1979.10489755, 1979.

Miller, R. L., Cakmur, R. V., Perlwitz, J., Geogdzhayev, I. V., Ginoux, P., Koch, D., Kohfeld, K. E., Prigent, C., Ruedy, R., Schmidt, G. A., and Tegen, I.: Mineral dust aerosols in the NASA Goddard Institute for Space Sciences ModelE atmospheric general circulation model, Journal of Geophysical Research Atmospheres, 111, 1–19, https://doi.org/10.1029/2005JD005796, 2006.

Mills, B. J. W., Krause, A. J., Scotese, C. R., Hill, D. J., Shields, G. A., and Lenton, T. M.: Modelling the long-term carbon cycle, atmospheric CO2, and Earth surface temperature from late Neoproterozoic to present day, Gondwana Research, 67, 172–186, https://doi.org/https://doi.org/10.1016/j.gr.2018.12.001, 2019.

Muhs, D. R.: The geologic records of dust in the quaternary, Aeolian Research, 9, 3–48, https://doi.org/10.1016/j.aeolia.2012.08.001, 2013.

Nguyen, H., Evans, A., Lucas, C., Smith, I., and Timbal, B.: The Hadley Circulation in Reanalyses: Climatology, Variability, and Change, Journal of Climate, 26, 3357–3376, https://doi.org/https://doi.org/10.1175/JCLI-D-12-00224.1, 2013.

Niedermeyer, E. M., Schefuß, E., Sessions, A. L., Mulitza, S., Mollenhauer, G., Schulz, M., and Wefer, G.: Orbital- and millennial-scale changes in the hydrologic cycle and vegetation in the western African Sahel: insights from individual plant wax δD and δ13C, Quaternary Science Reviews, 29, 2996–3005, https://doi.org/10.1016/J.QUASCIREV.2010.06.039, 2010.

Nowak, H., Vérard, C., and Kustatscher, E.: Palaeophytogeographical Patterns Across the Permian–Triassic Boundary, Frontiers in Earth Science, 8, 1–16, https://doi.org/10.3389/feart.2020.613350, 2020.

Pérez, C., Haustein, K., Janjic, Z., Jorba, O., Huneeus, N., Baldasano, J. M., Black, T., Basart, S., Nickovic, S., Miller, R. L., Perlwitz, J. P., Schulz, M., and Thomson, M.: Atmospheric dust modeling from meso to global scales with the online NMMB/BSC-Dust model – Part 1: Model description, annual simulations and evaluation, Atmospheric Chemistry and Physics, 11, 13 001–13 027, https://doi.org/10.5194/acp-11-13001-2011, 2011.

Price, G. D., Sellwood, B. W., and Valdes, P. J.: Sedimentological evaluation of general circulation model simulations for the "greenhouse" Earth: Cretaceous and Jurassic case studies, Sedimentary Geology, 100, 159–180, https://doi.org/https://doi.org/10.1016/0037-0738(95)00106-9, 1995.

Prospero, J. M., Ginoux, P., Torres, O., Nicholson, S. E., and Gill, T. E.: ENVIRONMENTAL CHARACTERIZATION OF GLOBAL SOURCES OF ATMOSPHERIC SOIL DUST IDENTIFIED WITH THE NIMBUS 7 TOTAL

OZONE MAPPING SPECTROMETER (TOMS) ABSORBING AEROSOL PRODUCT, Reviews of Geophysics, 40, 2–31, https://doi.org/https://doi.org/10.1029/2000RG000095, 2002.

Rea, D. K., Snoeckx, I., and Joseph, L. H.: Late Cenozoic Eolian deposition in the North Pacific: Asian drying, Tibetan uplift, and cooling of the northern hemisphere, Paleoceanography, 13, 215–224, https://doi.org/10.1029/98PA00123, 1998.

Royer, D. L., Berner, R. A., Montanez, I. P., Tabor, N. J., and Beerling, D. J.: CO2 as a primary driver of Phanerozoic climate, GSA Today, 14, 4–10, https://doi.org/10.1130/1052-5173(2004)014<4:CAAPDO>2.0.CO;2, 2004.

Sagoo, N., Valdes, P., Flecker, R., and Gregoire, L. J.: The early eocene equable climate problem: Can perturbations of climate model parameters identify possible solutions?, Philosophical Transactions of the Royal Society A: Mathematical, Physical and Engineering Sciences, 371, https://doi.org/10.1098/rsta.2013.0123, 2013.

Schepanski, K.: Transport of mineral dust and its impact on climate, Geosciences, 8, https://doi.org/10.3390/geosciences8050151, 2018.

Scotese, C. R.: PALEOMAP PaleoAtlas for GPlates and the PaleoData plotter program, PALEOMAP project, 2016.

Scotese, C. R. and Wright, N. M.: PALEOMAP Paleodigital Elevation Models (PaleoDEMS) for the Phanerozoic by Christopher R . Scotese and Nicky Wright Research School of Earth Sciences , Australian National University, pp. 1–26, https://www.earthbyte.org/paleodem-resource-scotese-and-wright-2018/, 2018.

Shao, Y.: A model for mineral dust emission, Journal of Geophysical Research Atmospheres, 106, 20 239–20 254, https://doi.org/10.1029/2001JD900171, 2001.

Soreghan, G. S., Soreghan, M. J., and Hamilton, M. A.: Origin and significance of loess in late Paleozoic western Pangaea: A record of tropical cold?, Palaeogeography, Palaeoclimatology, Palaeoecology, 268, 234–259, https://doi.org/10.1016/j.palaeo.2008.03.050, 2008.

Sugden, D. E., McCulloch, R. D., Bory, A. J., and Hein, A. S.: Influence of Patagonian glaciers on Antarctic dust deposition during the last glacial period, Nature Geoscience, 2, 281–285, https://doi.org/10.1038/ngeo474, 2009.

Tegen, I. and Fung, I.: Modeling of mineral dust in the atmosphere: sources, transport, and optical thickness, Journal of Geophysical Research, 99, 1994.

Turner, J. S. and Kraus, E. B.: A one-dimensional model of the seasonal thermocline I. A laboratory experiment and its interpretation, Tellus, 19, 88–97, https://doi.org/10.3402/tellusa.v19i1.9752, 1967.

Valdes, P. J., Armstrong, E., Badger, M. P., Bradshaw, C. D., Bragg, F., Crucifix, M., Davies-Barnard, T., Day, J., Farnsworth, A., Gordon, C., Hopcroft, P. O., Kennedy, A. T., Lord, N. S., Lunt, D. J., Marzocchi, A., Parry, L. M., Pope, V., Roberts, W. H., Stone, E. J., Tourte, G. J., and Williams, J. H.: The BRIDGE HadCM3 family of climate models: HadCM3@Bristol v1.0, Geoscientific Model Development, 10, 3715–3743, https://doi.org/10.5194/gmd-10-3715-2017, 2017.

Valdes, P. J., Scotese, C. R., and Lunt, D. J.: Deep ocean temperatures through time, Climate of the Past, 17, 1483–1506, https://doi.org/10.5194/cp-17-1483-2021, 2021.

Vallé, F., Westerhold, T., and Dupont, L. M.: Orbital-driven environmental changes recorded at ODP Site 959 (eastern equatorial Atlantic) from the Late Miocene to the Early Pleistocene, International Journal of Earth Sciences, 106, 1161–1174, https://doi.org/10.1007/s00531-016-1350-z, 2017.

Wade, D. C., Luke Abraham, N., Farnsworth, A., Valdes, P. J., Bragg, F., and Archibald, A. T.: Simulating the climate response to atmospheric oxygen variability in the Phanerozoic: A focus on the Holocene, Cretaceous and Permian, Climate of the Past, 15, 1463–1483, https://doi.org/10.5194/cp-15-1463-2019, 2019.

Wang, F., Li, Z., Sun, X., Zhao, J., Fan, Y., Xia, D., Ayyamperumal, R., and Li, B.: Early Cretaceous (late Barremian - Early Albian) expanding aeolian activity in East Asia: Evidence from the stratigraphic evolution of aeolian deposition in the Baiyin-Jingyuan Basin, northern China, GSA Bulletin, pp. 1–26, https://doi.org/10.1130/b36747.1, 2023.

Warren, J. K.: Evaporites through time: Tectonic, climatic and eustatic controls in marine and nonmarine deposits, Earth-Science Reviews, 98, 217–268, https://doi.org/10.1016/j.earscirev.2009.11.004, 2010.

Watterson, I. G., Bathols, J., and Heady, C. B. T. B. o. t. A. M. S.: What influences the skill of climate models over the continents? Simple skill scores for CMIP5 and CMIP3 climate models are analyzed for each continent and the globe, 95, 689+, https://link.gale.com/apps/doc/A376683387/AONE?u=anon~2463951d&sid=googleScholar&xid=e8a28062, 2014.

White, A. A. and Bromley, R. A.: Dynamically consistent, quasi-hydrostatic equations for global models with a complete representation of the Coriolis force, Quarterly Journal of the Royal Meteorological Society, 121, 399–418, https://doi.org/https://doi.org/10.1002/qj.49712152208, 1995.

Wilson, D.: Unified Model User Guide, chap. Precipitation, p. 32, in: Matthews, https://ukscience.org/_Media/UM_User_Guide.pdf, 1998.

Winckler, G., Anderson, R. F., Fleisher, M. Q., McGee, D., and Mahowald, N.: Covariant glacial-interglacial dust fluxes in the equatorial Pacific and Antarctica, Science, 320, 93–96, https://doi.org/10.1126/science.1150595, 2008.

Yang, Y., Galy, A., Fang, X., Yang, R., Zhang, W., Song, B., Liu, Y., Han, W., Zhang, W., and Yang, S.: Neodymium isotopic constraints on Cenozoic Asian dust provenance changes linked to the exhumation history of the northern Tibetan Plateau and the Central Asian Orogenic Belt, Geochimica et Cosmochimica Acta, 296, 38–55, https://doi.org/10.1016/j.gca.2020.12.026, 2021.

Zender, C. S., Newman, D., and Torres, O.: Spatial heterogeneity in aeolian erodibility: Uniform, topographic, geomorphic, and hydrologic hypotheses, Journal of Geophysical Research: Atmospheres, 108, https://doi.org/10.1029/2002jd003039, 2003.

Zhang, J., Liu, Y., Fang, X., Wang, C., and Yang, Y.: Large dry-humid fluctuations in Asia during the Late Cretaceous due to orbital forcing: A modeling study, Palaeogeography, Palaeoclimatology, Palaeoecology, 533, 109 230, https://doi.org/10.1016/j.palaeo.2019.06.003, 2019.

Zhang, W., Chen, J., Ji, J., and Li, G.: Evolving flux of Asian dust in the North Pacific Ocean since the late Oligocene, Aeolian Research, 23, 11–20, https://doi.org/10.1016/j.aeolia.2016.09.004, 2016.

Zhao, A., Ryder, C. L., and Wilcox, L. J.: How well do the CMIP6 models simulate dust aerosols?, Atmospheric Chemistry and Physics Discussions, 22, 1–32, https://doi.org/10.5194/acp-22-2095-2022, 2022.

Zhu, Z., Kuang, H., Liu, Y., Benton, M. J., Newell, A. J., Xu, H., An, W., Ji, S., Xu, S., Peng, N., and Zhai, Q.: Intensifying aeolian activity following the end-Permian mass extinction: Evidence from the Late Permian–Early Triassic terrestrial sedimentary record of the Ordos Basin, North China, Sedimentology, 67, 2691–2720, https://doi.org/10.1111/sed.12716, 2020.